

AperTO - Archivio Istituzionale Open Access dell'Università di Torino

**Kinematic and geochronological constraints on shear deformation  
in the Ferriere-Mollières shear zone (Argentera-Mercantour Massif,  
Western Alps): implications for the evolution of the Southern**

**This is a pre print version of the following article:**

*Original Citation:*

*Availability:*

This version is available <http://hdl.handle.net/2318/1660571> since 2018-02-23T11:09:39Z

*Published version:*

DOI:10.1007/s00531-018-1593-y

*Terms of use:*

Open Access

Anyone can freely access the full text of works made available as "Open Access". Works made available under a Creative Commons license can be used according to the terms and conditions of said license. Use of all other works requires consent of the right holder (author or publisher) if not exempted from copyright protection by the applicable law.

(Article begins on next page)

**Kinematic and geochronological constraints on shear deformation in the Ferriere-Mollières shear zone (Argentera-Mercantour Massif, Western Alps): implications for the evolution of the Southern European Variscan Belt**

Complete List of Authors:

Simonetti, Matteo\*;

*Università degli Studi di Torino, Dipartimento di Scienze della Terra, via V. Caluso 35, 10125 Torino, [matteo.simonetti@unito.it](mailto:matteo.simonetti@unito.it)*

ORCID ID: 0000-0002-8843-7615

Carosi, Rodolfo;

*Università degli Studi di Torino, Dipartimento di Scienze della Terra, via V. Caluso 35, 10125 Torino, tel. +39 0116705864, [rodolfo.carosi@unito.it](mailto:rodolfo.carosi@unito.it)*

ORCID ID: 0000-0002-6561-7090

Montomoli, Chiara;

*Università degli Studi di Pisa, Dipartimento di Scienze della Terra, via S. Maria 53, 56126 Pisa, tel. +390502215758, [chiara.montomoli@unipi.it](mailto:chiara.montomoli@unipi.it)*  
*IGG-CNR PISA, via Moruzzi 1, Pisa, Italy*

ORCID ID: 0000-0002-0364-5395

Langone, Antonio;

*IGG-CNR U.O.S. of Pavia, Via Ferrata 1, Pavia, Italy; [langone@crystal.unipv.it](mailto:langone@crystal.unipv.it)*

ORCID ID: 0000-0002-7346-2922

D'Addario, Enrico;

*Università degli Studi di Pisa, Dipartimento di Scienze della Terra, via S. Maria 53, 56126 Pisa; [endadda@gmail.com](mailto:endadda@gmail.com)*

Mammoliti, Elisa;

*Università degli Studi di Pisa, Dipartimento di Scienze della Terra, via S. Maria 53, 56126 Pisa; [elisamammoliti@ymail.com](mailto:elisamammoliti@ymail.com)*

\* Corresponding author [matteo.simonetti@unito.it](mailto:matteo.simonetti@unito.it)

**Kinematic and geochronological constraints on shear deformation in the Ferriere-Mollières shear zone (Argentera-Mercantour Massif, Western Alps): implications for the evolution of the Southern European Variscan Belt**

Simonetti M.<sup>a\*</sup>, Carosi R.<sup>a</sup>, Montomoli C.<sup>b,c</sup>, Langone A.<sup>d</sup>, D'Addario E.<sup>b</sup>, Mammoliti E.<sup>b</sup>

a) *Dipartimento di Scienze della Terra, Università di Torino, Via Valperga Caluso, 35, Torino, Italy;*

b) *Dipartimento di Scienze della Terra, Università di Pisa, Via S. Maria, 53, Pisa, Italy;*

c) *IGG-CNR PISA, via Moruzzi 1, Pisa, Italy;*

d) *IGG-CNR U.O.S. of Pavia, Via Ferrata 1, Pavia, Italy;*

\* Corresponding author Email: [matteo.simonetti@unito.it](mailto:matteo.simonetti@unito.it)

**Abstract**

In the Western Alps a steeply dipping km-scale shear zone (the Ferriere-Mollières shear zone) cross-cuts Variscan migmatites in the Argentera-Mercantour External Crystalline Massif.

Structural analysis joined with kinematic vorticity and finite strain analyses allowed to recognize a high-temperature deformation associated to dextral transpression characterized by a variation in the percentage of pure shear and simple shear along a deformation gradient. U-Th-Pb dating of syn-kinematic monazites was performed on mylonites. The oldest ~340 Ma ages were obtained in protomylonites whereas ages of ~ 320 Ma were found in mylonites from the core of the shear zone. These ages indicate that the Ferriere-Mollières shear zone is a still preserved Variscan shear zone.

Ages of ~320 Ma obtained in this work are in agreement with ages of the dextral transpressional shear zones occurring in the Maures-Tanneron Massif and Corsica-Sardinia. However, transpression in the Argentera-Mercantour Massif started earlier than in other sectors of the southern Variscan Belt. This is possibly caused by the curvature of the belt triggering the progressive migration of shear deformation. Our data allow a correlation between the Argentera-Mercantour Massif and other segments of the Southern European Variscan Belt, in particular with Maures-Tanneron Massif and Corsica-Sardinia and contribute to fill a gap in the age of activity and in the kinematics of the flow of the system of dextral shear zones of the southern portion of the EVSZ.

**Key words:** Transpression, Argentera-Mercantour Massif, Mylonites, East Variscan Shear Zone, Monazite

## 69    **1. Introduction**

70    The European Variscan Belt is the result of a Devonian–Carboniferous continent-continent collision (Arthaud and  
71    Matte, 1977; Burg and Matte, 1978; Tollmann, 1982; Matte, 1986a,b; Franke, 1989) between Laurentia-Baltica and  
72    Gondwana (Matte, 1986a, 2001). Between these two continents, small microplates existed, defined essentially on the  
73    basis of palaeomagnetism and palaeobiostratigraphy (Scotese and McKerrow, 1990; Franke et al., 2017, with references  
74    therein). The main microplates are known as Avalonia and Armorica (Matte, 2001). They broke away from Gondwana  
75    during the early Palaeozoic, prior to docking against Baltica and Laurentia before the Devonian-Carboniferous collision  
76    (Matte, 2001).

77    The Architecture of the Variscan Belt is well defined in eastern, central and western Europe (Matte, 1986b, 2001; Fluck  
78    et al., 1991; Ballèvre et al., 2009; Faure et al. 2009; Skrzypek et al., 2012) where the Saxothuringian Zone  
79    (southwestern Iberian Massif, northern Armorican Massif, Vosges and Bohemian Massif) and the Moldanubian Zone  
80    (southern Iberian Massif, central and southern Vosges, Massif Central, southern Armorican Massif and southern  
81    Bohemian Massif) are recognized (Fig. 1a).

82    In contrast, the structural arrangement of the SE segment of the European Variscan Belt is less clear because of tectonic  
83    reworking during Alpine Orogeny.

84    Some authors proposed that the European Variscan Belt is characterized by a composite orocline, developed because of  
85    indentation tectonics (Matte and Ribeiro, 1975; Matte, 1986a,b), made by two main branches: the well-known western  
86    Ibero–Armorican arc (Matte and Ribeiro, 1975; Brun and Burg, 1982; Dias and Ribeiro, 1995; Dias et al., 2016;  
87    Fernández-Lozano et al., 2016) and the eastern branch (Matte, 2001; Bellot, 2005), delimited by a system of regional-  
88    scale dextral, transpressive shear zones known as the East Variscan Shear Zone (EVSZ; Corsini and Rolland, 2009;  
89    Carosi et al., 2012; Padovano et al., 2012, 2014). The EVSZ is actually less understood, especially in the sectors that  
90    are now part of the Alps.

91    Although during the Carboniferous extensive transpressive shear deformation is recognized in several fragments  
92    belonging to the Southern European Variscan Belt (Matte, 1986a,b; Carosi and Palmeri, 2002; Iacopini et al., 2008;  
93    Frassi et al., 2009; Carosi et al., 2012; Corsini and Rolland, 2009; Guillot et al., 2009; Schneider et al., 2014), the  
94    impact of this deformation on the arrangement of the belt needs further constraints.

95    A deeper knowledge of Variscan deformation is of great importance for enhancing correlations between the fragments  
96    of the belt in the Mediterranean area since these correlations are mostly based on lithological and stratigraphic affinities  
97    and paleomagnetic data. In particular, the correlation between Corsica-Sardinia Block, Maures-Tanneron Massif and  
98    Variscan basement of the Western Alps (External Crystalline Massifs) is still debated. According to some authors these  
99    three sectors should have been in continuity during Variscan orogenesis (Rollet et al., 2002; Rosenbaum et al., 2002;

Advokaat et al., 2014), while according to Stampfli et al. (2002), Turco et al. (2012), von Raumer et al. (2013), the Corsica-Sardinia Block was located in a more westerly position connected to Iberia and therefore, away from southern France and the future Alpine External Crystalline Massifs.

In the Western Alps, the Variscan External Crystalline Massifs are cross-cut by km-scale shear zones whose age of activity and deformation regime are not entirely clear. It is also not clear whether these shear zones have been fully reactivated during the Alpine orogeny, or if evidence of Variscan deformation is still preserved.

A useful method to date shear zone activity, especially when developed under high-temperature conditions, is the U-Th-Pb geochronology on syn-kinematic monazite (Williams et al., 2007). Reliable results were obtained in the Himalayan belt in dating both the activity of regional-scale shear zones (Carosi et al., 2010; Montomoli et al., 2013, 2015; Cottle et al., 2015; Iaccarino et al., 2015, 2017; Carosi et al., 2016a) and metamorphic events (Khon et al., 2005; Khon, 2008; Larson and Cottle, 2015). In high-temperature shear zones, this method is more reliable than the  $^{40}\text{Ar}/^{39}\text{Ar}$  method because argon isotopes are often mobile during deformation (Dunlap et al., 1991; Mulch and Cosca, 2004; Villa et al., 1997, 2014; Villa, 2015; Challandes et al., 2003, 2008; Sanchez et al., 2011).

In the present work we focus on the northern sector of the Ferriere-Mollières shear zone (FMSZ; Faure-Muret, 1955; Malaroda et al., 1970; Compagnoni et al., 2010) located in the Argentera-Mercantour Massif, a km-scale shear zone in the Alpine External Crystalline Massifs. The FMSZ is constituted by mylonites developed from Variscan migmatites and leucogranites (Musumeci and Colombo, 2002; Carosi et al., 2016b). Conflicting deformation ages have been proposed: Musumeci and Colombo (2002) obtained a cooling age for mylonitic leucogranite of  $327 \pm 3$  Ma (whole rock Rb/Sr ages on magmatic muscovite grains) interpreted as the younger limit of the FMSZ activity. Corsini et al. (2004) and Sanchez et al. (2011) proposed deformation ages of  $\sim 22$  and  $\sim 20$  Ma ( $^{40}\text{Ar}/^{39}\text{Ar}$  on phengites from mylonitic micaschists and from ultramylonites of the Argentera granite), suggesting a reactivation of the Variscan shear zone (e.g. Valetta shear zone) and formation of new shear zones (e.g. Fremamorta-Colle del Sabbione shear zone) during Alpine orogeny under greenschist metamorphic conditions.

This paper aims to clarify both the kinematics of the flow and the age of activity of the FMSZ in order to check if Variscan deformation structures are still preserved and if dextral shear deformation affecting the Alpine External Crystalline Massifs can be linked to the activity of other similar transpressional shear zones in the Southern European Variscan Belt. To verify this hypothesis, we carried out a kinematic vorticity analysis and a U-Th-Pb geochronological study on syn-kinematic monazites, combined with structural and microstructural analyses on different types of mylonites recently mapped by Carosi et al. (2016b).

## 130    **2. Geological Setting of the Argentera-Mercantour Massif**

131    The External Crystalline Massifs in the Western Alps are, together with the Corsica-Sardinia Block and the Maures-  
132    Tanneron Massif, fragments of the Variscan Belt well-preserved within the Mediterranean area.

133    The Argentera-Mercantour Massif is constituted by the Gesso-Stura-Vésubie (GSV) and the Tinée (TMC) metamorphic  
134    complexes (Malaroda et al., 1970; Compagnoni et al., 2010) which are separated by the FMSZ (Fig. 1b). The GSV  
135    complex is made of migmatitic gneiss derived from Late Ordovician granitoids and migmatitic paragneiss. Ferrando et  
136    al. (2008) and Compagnoni et al. (2010) recognized a metamorphic evolution characterized by: 1) HP metamorphic  
137    peak; 2) initial decompression stage; 3) HT–MP amphibolite-facies metamorphism; 4) LT–LP amphibolite-facies  
138    metamorphism.

139    The TMC migmatites resulted from partial melting of metasediments. Eclogite relicts are reported by Faure-Muret  
140    (1955) and Malaroda et al. (1970). According to Compagnoni et al. (2010) the TMC shows a minor degree of melting  
141    than the migmatites of the GSV complex as testified by a smaller proportion of leucosomes. A greenschist facies  
142    imprint is mainly due to a system of ductile to brittle-ductile shear zones (Baietto et al., 2009) affecting the whole  
143    Argentera-Mercantour Massif (Corsini et al., 2004; Sanchez et al., 2011). The main Alpine faults of the Argentera-  
144    Mercantour Massif are the NW-SE Bersezio Fault Zone, in the central part, and the E-W Fremamorta-Colle Sabbione  
145    Shear Zone, in the southernmost part of the massif (Fig. 1b).

146    The FMSZ (also known as Valletta shear zone; Corsini et al., 2004) strikes NW–SE and extends for about 20 km (Fig.  
147    1b) with a thickness between 100 m to the south-east and more than 1000 m to the north-west. The fault rocks in the  
148    FMSZ resulted from the shearing of migmatites of the GSV and the TMC. The transition from non-sheared migmatites  
149    to protomylonites, mylonites and ultramylonites can be observed along a deformation gradient towards the center of the  
150    shear zone (Fig. 2; Carosi et al., 2016b). The rocks in the shear zone are medium-grained dark mylonitic schists with  
151    biotite and white mica  $\pm$  garnet. Mylonites and ultramylonites with chlorite and white mica also occur in the central part  
152    of the shear zone while mylonites and protomylonites with biotite and sillimanite  $\pm$  garnet are present in the margins of  
153    the shear zone. Because of the constant orientation of the mylonitic foliation, the mineral lineation and the sense of  
154    shear in all the rocks inside the FMSZ, Carosi et al. (2016b) interpreted these parageneses as linked to an evolution of  
155    the deformation under decreasing temperature.

156

## 157    **3. Structural Analysis**

158

### 159    **3.1 Variscan shear zone**

160 The main structural elements in the FMSZ are a mylonitic foliation defined by the preferred orientation of biotite +  
 161 white mica and a protomylonitic foliation with biotite + sillimanite in the external part of the shear zone, both striking  
 162 N100-140 and steeply dipping towards the northeast or the southwest (Fig. 2). A mineral lineation, defined by a  
 163 preferred alignment of stretched quartz and feldspar, trends N110-130 and dips 20° towards the northwest (Fig. 2).  
 164 In protomylonites the foliation is an anastomosed disjunctive cleavage (Passchier and Trouw, 2005) formed by  
 165 alternating coarse-grained layers of deformed quartz and feldspar and biotite- and sillimanite-rich layers (Fig. 3a,b).  
 166 Sillimanite occurs both in prismatic and fibrolitic habitus. In the mylonites, a transition can be observed from a  
 167 disjunctive cleavage with sub-parallel cleavage domains, formed by alternating layers of deformed quartz and biotite +  
 168 white mica (Fig. 3c,d), to a continuous cleavage in the most intensely deformed ultramylonites rich in phyllosilicates  
 169 (Fig. 3e,f). The mylonitic foliation underwent a later gentle folding of uncertain age with axial planes moderately  
 170 dipping toward the SW and NW-SE trending axes (Fig. 2). Kinematic indicators (S-C' fabric, micafish, mantled  
 171 porphyroclasts and quartz oblique foliation) indicate a strike-slip component of movement with a minor reverse, top-to-  
 172 the-SE, component where the foliation dips northeast (Fig. 4a,b,c) and with a minor normal component where it dips  
 173 southwest. Quartz shows subgrain rotation recrystallization (Piazolo and Passchier, 2002; Stipp et al., 2002) and only  
 174 very minor effects of grain boundary migration in mylonites (Fig. 4d) and ultramylonites. Quartz in protomylonites is  
 175 mainly affected by grain boundary migration (Piazolo and Passchier, 2002; Stipp et al., 2002). Feldspar shows undulose  
 176 extinction due to ductile deformation (Fig. 4e) and does not show evidence of brittle deformation. The thickness of the  
 177 FMSZ progressively decreases from NW to SE. The maximum thickness of ~2 km is reached to the NW, in the Ferriere  
 178 village area (Fig. 1b). Thickness variations of the different types of mylonites, at a local scale, were also reported (in  
 179 agreement with Carosi et al., 2016b, Fig. 2). In the wall rocks of the FMSZ, in the GSV and TMC complex, Carosi et al.  
 180 (2016b) and Simonetti et al. (2017) recognized outcrop-scale open to tight symmetric upright folds with NW-SE  
 181 oriented axial plane and NW dipping axis deforming the main foliation of the migmatites.

182

183

### 184 3.2 Alpine Shear Zones

185 Shear zones cross-cutting the mylonites of the FMSZ (Fig. 2) and the migmatites of the two metamorphic complexes  
 186 have been identified (Fig. 5a). These shear zones have metric to decametric thickness with lateral continuities up to  
 187 several hundred meters. They consist of fine-grained mylonites or phyllonites with quartz and feldspar porphyroclasts in  
 188 a fine-grained chlorite + white mica matrix. This paragenesis is indicative of greenschist facies metamorphism. Biotite  
 189 relicts, indicating an older, higher temperature foliation, are still recognizable. The proportion of matrix is ~ 65% -

190 75%. The foliation strikes nearly E-W and dips at moderate to low angles toward the north with a north plunging  
191 mineral lineation.

192 The foliation is a spaced cleavage defined by the preferred orientation of chlorite and white mica. Kinematic indicators,  
193 mainly micafish and S-C and S-C' fabrics, indicate a top-to-the-S reverse sense of shear (Fig. 5b). C and C' planes are  
194 characterized by the presence of fine-grained chlorite. Along the S foliation biotite relicts are sometimes present (Fig.  
195 5c). Quartz shows undulose extinction and subgrains, the latter indicating subgrain rotation recrystallization (Piazolo  
196 and Passchier, 2002; Stipp et al., 2002) as the dominant deformation mechanism. Feldspar shows undulose extinction  
197 and deformation lamellae while some fractured porphyroclasts are also present.

198

#### 199 **4. Kinematics and vorticity of the flow of the FMSZ**

200 Deformation in shear zones is often approximate to simple shear, especially in high-strain zones (Passchier 1987, 1991;  
201 Iacopini et al., 2010, 2011). However, a significative component of pure shear has been detected in many regional-scale  
202 shear zones around the world, under various metamorphic conditions (Carosi and Palmeri, 2002, Carosi et al., 2005;  
203 Carosi et al., 2006, 2007; Festa et al., 2016; Goscombe et al., 2003, 2005; Iacopini et al., 2008; Kurz and Northrup,  
204 2008; Larson and Godin, 2009; Law et al., 2004; Li et al., 2016; Nabavi et al., 2016; Sarkarinejad and Azizi, 2008;  
205 Sarkarinejad et al., 2015; Wu et al., 2016; Xypolias and Kokkalas, 2006; Zang and Teyssier, 2013).

206 In order to characterize the type of flow and the deformation of the FMSZ, a kinematic vorticity analysis was performed  
207 on mylonites collected along three transects (A, B and C) perpendicular to the shear zone boundaries and parallel to the  
208 deformation gradient (Fig. 6). In addition, we performed a finite strain analysis in order to obtain the axial ratio of the  
209 finite strain ellipsoid ( $R_{xz}$ ), which is indispensable for calculating the shortening perpendicular to the flow plane.

210

#### 211 **4.1 Methods**

212 Pure and simple shear can be expressed through the dimensionless mean kinematic vorticity number ( $W_m$ ). Within a  
213 ductile flow, the non-coaxial component of deformation, defined vorticity, can be normalized to the stretching along the  
214 strain axes in order to obtain a dimensionless number that allows to compare the different types of flow. In this way it is  
215 possible to define the kinematic vorticity number as  $W_k = W/|d_2 - d_3|$  (Passchier, 1987).  $W$  represents the vorticity and  
216  $d_2 - d_3$  represents the difference of stretching along the intermediate and minimum principal strain axes. The mean  
217 kinematic vorticity number  $W_m$  can be assumed equal to  $W_k$  because it represents an average value over the  
218 deformation interval during which the structure or fabric formed (Xypolias, 2010; Fossen and Cavalcante, 2017).  $W_m$  is  
219 therefore a measure of the proportion of pure and simple shear components:  $W_m = 0$  for pure shear;  $W_m = 1$  for simple



220 shear;  $0 < W_m < 1$  for general shear (Passchier, 1987). Simple and pure shear contribute equally to the flow for a value of  
 221  $W_m = 0.71$  (Law et al., 2004; Xypolias, 2010).

222 The kinematic vorticity analysis was carried out on thin sections oriented parallel to the XZ plane of the finite strain  
 223 ellipsoid.

224 It was performed using the S-C' method (Kurz and Northrup, 2008), which is based on the measurement of the  
 225 orientation of C' planes (Fig. 7a) with respect to the shear zone boundary. In any type of flow it is possible to recognize  
 226 two lines, defined as flow apophyses (A1 and A2), along which the particles do not undergo rotation. The component of  
 227 simple shear decreases with the angle between the two apophyses: the flow apophyses are orthogonal for pure shear  
 228 flow, and coincide with each other for simple shear flow. For general shear flow A1 and A2 form an acute angle in the  
 229 direction of the flow (Fig. 7a). The C' plane represents the bisector of the angle  $2v$  between the A1 and A2 flow  
 230 apophyses (Fig. 7a; e.g. Kurz and Northrup, 2008). The vorticity number can be derived through the relation  $W_k =$   
 231  $\cos 2v$  (Kurz and Northrup, 2008) where  $v$  is the angle between C' and C planes that assumed are parallel to the flow  
 232 apophysis A2 (Kurz and Northrup, 2008; Gillam et al., 2013). Following the procedure proposed by Gillam et al.  
 233 (2013), we measured the  $v$  angle since the mylonitic foliation has a constant trend, sub-parallel to the well-defined and  
 234 mapped shear zone boundaries (Carosi et al., 2016b), in the studied transects.

235 As each element in a flow tends to rotate, including C' planes, it is necessary to consider the largest value for  $v$ , among  
 236 those measured, to estimate the initial amplitude of the angle during formation of the C' planes. Gillam et al. (2013)  
 237 proposed to use an average value of the angle  $v$  for low-strain rocks or in cases where C' planes developed in a late  
 238 stage of the deformation history and nucleated in a stable orientation, as in this case they underwent  
 239 little or no rotation after inception. For highly strained rocks deformed in long lasting shear zones the maximum value  
 240 of  $v$  is preferable because, as demonstrated by Kurz and Northrup (2008), the average value is not representative of the  
 241 original angle of nucleation of C' planes.

242 Finite strain analysis has been performed on the XZ section of oriented samples applying the center-to-center method  
 243 (Fry, 1979). The analysis was performed on samples in which an adequate amount of feldspar porphyroclasts with a  
 244 similar grain size are present. Feldspar porphyroclasts show a homogeneous distribution in the samples used for the  
 245 analysis and therefore are in agreement with the fundamental assumption of the method (see Genier and Epard, 2007 for  
 246 a critical review). The center-to-center analysis was carried out using the software EllipseFit 3.2 (Vollmer, 2005).

247 The data obtained from strain and vorticity analyses were combined using the equations proposed by Wallis et al.  
 248 (1993) and Law et al. (2004) to obtain the percentages of shortening and stretching of the shear zone (Fig. 7b).

249 In order to check the kinematics and the type of deformation of the shear zone we calculated the angles  $\theta$ , between the  
 250 maximum Instantaneous Stretching Axis ( $ISA_{max}$ ) in the horizontal plane and the shear zone boundary, as this parameter

appears to be fundamental to distinguish between transpression and transtension, according to Fossen and Tikoff (1993) and Fossen et al. (1994).  $\theta$  angles larger than  $45^\circ$  are indicative of transtensive deformation while  $\theta$  angles smaller than  $45^\circ$  are indicative of transpressional deformation.

The calculation was performed using the formula proposed by Xypolias (2010) according to which  $Wk = \sin 2\theta$  and consequently  $\theta = (\arcsin Wk)/2$ . Results were checked with the software Strain Calculator 3.2 (Holcombe, 2009).

#### 4.2 Results of vorticity and strain analyses

Results of vorticity and strain analyses are reported in table 1, polar histograms used to derive the angle  $\nu$  are reported in figure 8 and Fry graphs of the XZ section are reported in figure 9. In each of the three transects the estimated  $Wk$  values are very similar taking into account the degree of deformation of the samples. In protomylonites (samples: ARG 144, ARG 143, ARG 19)  $Wk$  varies from 0.32 to 0.34. In mylonites (samples: ARG 45, ARG 21a, ARG 68, ARG 116, ARG 117, ARG 115)  $Wk$  varies between 0.37 and 0.69. In ultramylonites (samples: ARG 35, ARG 101, ARG 37, ARG RCV, ARG 41)  $Wk$  is variable between 0.81 and 0.89. It is therefore possible to observe a change in the value of  $Wk$  along the deformation gradient toward the center of the shear zone.

Finite deformation analysis, combined with  $Wk$  values, allowed to obtain shortening and stretching values quite concordant in all the studied samples: shortening varies from 19% to 37% with an average value of 27%; stretching ranges from 23% to 59% with an average value of 36%.  $\theta$  varies from  $9^\circ$  in protomylonites to  $31^\circ$  in ultramylonites.

#### 5. Geochronology

In-situ U-Th-Pb analyses were performed with LA-ICP-MS on monazites in five samples (ARG 19, ARG 21, ARG 27, ARG 29, ARG 48b) collected along the deformation gradient of the shear zone along the crest of Costabella del Piz (Fig. 6c). Sample ARG 19 is a protomylonite derived from biotite- and sillimanite-bearing migmatite. Samples ARG21, ARG 27, ARG 29 and ARG 48b are mylonites derived from biotite- and white mica-bearing migmatites.

Dating was performed following the analytical procedure suggested by Montomoli et al. (2013). First, minerals with high relief and high birefringence were located using the optical microscope. Subsequently the samples were polished and C-coated to be inspected using a Scanning Electron Microscope (JEOL JSM IT300LV), at the University of Torino (Italy), which allows to distinguish monazite from zircon. On grains selected for dating (examples reported in figure 10), quantitative chemical analyses, reported in Online Resource 1 (spots reported in figure 11), and compositional maps (Fig. 11) were acquired by using electronic microprobe (JEOL 8200 Super Probe), at the University of Milano (Italy), in order to highlight any compositional zoning.

Monazite grains were analyzed in situ by laser-ablation inductively coupled plasma mass spectrometry (LA-ICP-MS) on 30- $\mu$ m-thick sections at the CNR-Istituto di Geoscienze e Georisorse U.O. Pavia (Italy) using an Ar-F 193-nm excimer laser (GeolLas 102 from Micro-Las) coupled with a magnetic sector ICP-MS (Element I from ThermoFinnigan). The full description of the analytical procedures is reported in Paquette and Tiepolo (2007) and Tiepolo (2003). Single analyses were performed by a one-minute acquisition of the background signal followed by recording, for at least 30 seconds, the ablation signal of the masses:  $^{202}\text{Hg}$ ,  $^{204}(\text{Hg}+\text{Pb})$ ,  $^{206}\text{Pb}$ ,  $^{207}\text{Pb}$ ,  $^{208}\text{Pb}$ ,  $^{232}\text{Th}$  and  $^{238}\text{U}$ . The presence of common Pb was evaluated in each analysis on the basis of the net signal of  $^{204}\text{Pb}$  (i.e. subtracted for the interference of  $^{204}\text{Hg}$  and background). None of the samples gave  $^{204}\text{Pb}$  counts above the background level. However the relatively high Hg signal in the gas blank does not exclude the effective presence of common Pb in the analyzed monazites. Analytical conditions were 10  $\mu$ m diameter of spot size, 8 J/cm<sup>2</sup> of energy density, and 3 Hz of repetition rate. Time-resolved signals were carefully inspected to verify the presence of perturbations related to inclusions, fractures or mixing of different age domains. Laser-induced elemental fractionation and mass bias were corrected using matrix-matched external monazite standard (Moacir monazite: Cruz et al., 1996; Seydoux-Guillaume et al., 2002a,b) considering the values, re-calibrated for isotopic disequilibrium, reported by Gasquet et al. (2010). Eight to nine external standards were analyzed in each analytical run and only those close to the reference values (at least 4 in each run) were considered in order to reduce errors related to the standard reproducibility (Table 2). The relative standard deviation of the analyses was mostly within 2 % – 4 %. External standards and unknowns were integrated over the same time intervals to ensure the efficient correction of fractionation effects. Data reduction was carried out with the GLITTER® software (van Achterbergh et al., 2001). In order to better estimate the uncertainty affecting the  $^{206}\text{Pb}/^{238}\text{U}$ ,  $^{207}\text{Pb}/^{235}\text{U}$  and  $^{208}\text{Pb}/^{232}\text{Th}$  isotope ratios, the external reproducibility of the standard was propagated relative to individual uncertainties for the isotope ratios. This procedure was carried out for each analytical run as reported in Horstwood et al. (2003). After this error propagation each analysis is accurate within the quoted errors. Data processing and plotting was done with the macro ISOPLOT/Ex (Ludwig, 2003).

## 5.1 Characterization of the Monazites

Monazite belongs to the family of orthophosphates with general formula  $\text{A}(\text{PO}_4)$  and is an anhydrous rare earth phosphate (Williams et al., 2007). Monazite is ideal for recording the progress of geological processes, because with its extremely variable composition it reflects the chemical and physical changes of the host rocks and preserves the age of crystallization or growth over long geological periods (Williams et al., 2007). It is ideal for the U-Th-Pb method because it can have large concentrations of U and Th but does not incorporate Pb during its formation.

312 In systems in which the monazite is associated with garnet it is possible to observe partition phenomena of Y and HREE  
313 between these two phases (Williams et al., 2007). After xenotime, garnet is the main mineral that can accommodate  
314 HREE and Y in metamorphic rocks and its growth or its destabilization strongly influence the distribution of Y and  
315 HREE in metamorphic monazites (Pyle and Spear, 1999; Pyle et al., 2001): during prograde metamorphism Y tends to  
316 enter preferentially in garnet while during retro-metamorphism Y tends to enter preferentially in monazite (Pyle and  
317 Spear, 1999; Pyle et al., 2001; Williams et al., 2007). The microstructural study, combined with the analysis of the  
318 variation of the composition of monazites in deformed rocks, allows to understand in which moment of the deformation  
319 history the two phases have grown.

320 Monazites were analyzed for microstructural position (examples of monazites located in different structural positions  
321 are reported in figure 10) and the Y content and zoning highlighted by the compositional maps acquired by electron  
322 microprobe. In both protomylonite (ARG 19) and mylonites (ARG 21, ARG 27, ARG 29, ARG 48b) no xenotime  
323 crystals have been detected and cores of the monazites have often a lower Y content with respect to the rims. Some  
324 monazites have asymmetrical shapes. Monazites in mylonites show irregular and frayed edges with asymmetric rims  
325 constituted by allanite  $\pm$  apatite often developed in extensional sites around the crystals.

326

## 327 5.2 U-Th-Pb results

328 U-Pb data (Table 3) provide mainly discordant ages, with eight concordant U-Pb ages ranging from 348 to 297 Ma (Fig.  
329 12). Except for ARG 19 protomylonite,  $^{206}\text{Pb}/^{238}\text{U}$  and  $^{208}\text{Pb}/^{232}\text{Th}$  data yield more concordant ages (Table 3, Fig. 12).  
330 Both  $^{206}\text{Pb}/^{238}\text{U}$  and  $^{208}\text{Pb}/^{232}\text{Th}$  ages range mainly from 340 to 320 Ma and define a broad rejuvenation trend from the  
331 least deformed sample (ARG 19 protomylonite) to highly sheared samples in the core of the shear zone (Fig. 12).  
332 We did not note a systematic correlation between ages and monazite chemical domains. The oldest U-Th-Pb ages were  
333 obtained from a monazite grain included in garnet ( $>400$  Ma; Mnz 59, sample ARG 48b) and a monazite grain included  
334 in a deformed white mica ( $^{206}\text{Pb}/^{238}\text{U}$  age of  $374 \pm 6$  Ma; Mnz 9, ARG 29), suggesting a textural control and inheritance  
335 of the obtained ages.

336

337

## 338 6. Discussion

339 The FMSZ is a steeply dipping shear zone with a main right-lateral reverse top-to-the-SE sense of shear, whereas  
340 locally it shows a normal sense of shear, depending on the dip direction of the mylonitic foliation. The FMSZ  
341 developed under conditions of decreasing temperature, starting from the HT amphibolite facies to at least the LT  
342 amphibolite facies, as suggested by the presence of sillimanite + biotite and biotite + white mica along the

343 protomylonitic and mylonitic foliations, respectively. The geometry of the foliation and mineral lineation as well as the  
 344 kinematic indicators are concordant in the protomylonites and in the mylonites. Temperature during Alpine deformation  
 345 was  $375 \pm 30$  °C (greenschist facies metamorphism; Corsini et al., 2004; Sanchez et al., 2010) and, as a consequence,  
 346 the amphibolite-facies metamorphism may be inferred to be pre-Alpine.

347 The results allowed us to define for the first time the deformation regime and the finite strain of the FMSZ.

348 The kinematic vorticity data obtained by the S-C' method (Kurz and Northrup, 2008) allowed us to quantify the  
 349 deformation, characterized by a non-coaxial flow, in terms of percentage of pure and simple shear components.

350 Samples from the less deformed lithotypes, localized in the external portion of the shear zone, record a deformation  
 351 dominated by pure shear. The amount of simple shear increases towards the center of the shear zone, from ~24 % in the  
 352 protomylonites to ~ 62% in the ultramylonites (Fig. 13a). Finite strain analysis yields average shortening and stretching  
 353 values of 27 % and 36 %, respectively.

354 Taking into account the type of flow, the finite strain and the angles  $\theta$  between the maximum horizontal ISA and the  
 355 shear zone boundaries (Fig. 13b), we can recognize a change from a pure shear dominated transpression to a simple  
 356 shear dominated transpression (Fig. 13c) according to the models proposed by Fossen and Tikoff (1993) and by Fossen  
 357 et al. (1994). The attitude of the mylonitic foliation is sub-vertical along the 20 km length of the shear zone, in  
 358 accordance with a transpressive shear zone setting (Fossen et al., 1994; Fossen, 2016). In the case of transtensional  
 359 deformation as suggested by Musumeci & Colombo (2002), the attitude of mylonitic foliation is expected to be sub-  
 360 horizontal due to the main sub-vertical shortening direction. Iacopini et al. (2008), discussing the orientations of the  
 361 elongation lineation, suggest two kinds of transpressive shear zones: in the case of a sub-vertical lineation the shear  
 362 zone was subjected to vertical extrusion while in the case of a sub-horizontal lineation extrusion was horizontal. The  
 363 elongation lineation within the FMSZ is gently plunging, thus it would be compatible with a sub-horizontal direction of  
 364 extrusion. Extrusion and shear zones with a component of pure shear are generally subjected to strain compatibility  
 365 problems (Hudleston, 1999) and it is not trivial to explain how the flattening component of the deformation is  
 366 accommodated.

367 To fix this problem Ramsay and Huber (1987) and Hudleston (1999) suggested that the flattening component can be  
 368 obtained in a simple shear regime by volume loss in the deforming material. In this way the strain compatibility is  
 369 maintained. However, this is not the case of the FMSZ because there is no evidence of structures suggesting major  
 370 volume loss in the deformed rocks and the kinematic vorticity analysis revealed a major component of pure shear  
 371 during deformation.

372 Anyway, according to Fossen (2016) strain compatibility problems are also overcome if the wall rocks are deformed by  
 373 the same amount of coaxial strain as the shear zone. The wall rocks of the FMSZ, i.e. the GSV and the TMC complexes

are deformed by open to tight upright folds with axial planes parallel to the mylonitic foliation in the FMSZ. According to Carosi et al. (2016b) and Simonetti et al. (2017) these upright folds accommodate the component of shortening perpendicular to the FMSZ. According to this, the wall rocks and the shear zone could stretch together with no strain compatibility problems.

The Argentera-Mercantour Massif was involved in the Alpine orogeny at ~22 Ma (Corsini et al., 2004, Sanchez et al., 2011). Most of the Alpine deformation is concentrated in the sedimentary covers, detached from the metamorphic basement along gypsum and limestone breccias levels (Malaroda et al., 1970), in which several folding phases are recognizable (d'Atri et al., 2016; Barale et al., 2016). Evidence of Alpine deformation in the basement are brittle/ductile strike-slip faults and top-to-the-S reverse shear zones developed under greenschist facies conditions during the lower Miocene (Corsini et al., 2004; Baietto et al., 2009). Variscan HT foliation and mylonitic foliation in the FMSZ all along its length are always subvertical and are not affected by strong subsequent folding.

U-Th-Pb geochronology on monazites provides no Alpine ages showing that the shear zone was not significantly reactivated during the Alpine orogeny. U-Pb data are discordant whereas the  $^{206}\text{Pb}/^{238}\text{U}$  and  $^{208}\text{Pb}/^{232}\text{Th}$  ages show a better concordance. As recently demonstrated by Erickson et al. (2015), the perturbation of the U-Th-Pb systematics of monazite can be caused by intracrystalline deformation. We interpret the obtained geochronological data combining textural observations, monazite chemistry and age distribution. The oldest U-Th-Pb ages were obtained from monazite grains included in garnet (Fig. 10a) and within a deformed white mica (Fig. 10b). These grains probably escaped subsequent deformation and other events perturbing the U-Th-Pb systematics. They can be interpreted as inherited ages from older tectono-metamorphic events as previously documented by other authors (Monié and Maluski 1983; Rubatto et al. 2001; Corsini et al. 2004).

The  $^{206}\text{Pb}/^{238}\text{U}$  and  $^{208}\text{Pb}/^{232}\text{Th}$  ages range mainly from about 340 to 320 Ma. The oldest  $^{206}\text{Pb}/^{238}\text{U}$  ages of this range were obtained in monazites along the protomylonitic foliation (Fig. 10c) close to the margin of the shear zone. This age, according to the syn-kinematic mineral assemblage and to the main deformation mechanism of quartz and feldspar, suggests that Variscan shear deformation in the Argentera-Mercantour Massif started at the metamorphic peak (dated at ~340 Ma in the GSV complex, Compagnoni et al., 2010; Rubatto et al., 2010) or shortly after it during the first partial melting event and triggered the exhumation of the GSV complex.

Both  $^{206}\text{Pb}/^{238}\text{U}$  and  $^{208}\text{Pb}/^{232}\text{Th}$  ages become younger along the deformation gradient (Fig. 14) and monazite grains along the mylonitic foliation in the core of the shear zone (Fig. 10d) show  $^{206}\text{Pb}/^{238}\text{U}$  and  $^{208}\text{Pb}/^{232}\text{Th}$  ages of  $\sim 320 \pm 6$  Ma. This broad correlation between ages and deformation gradient suggests a progressive concentration of deformation into the center of the shear zone.

404 This is in agreement with the type II shear zone growth-model proposed by Fossen (2016). Here deformation localizes  
 405 in the central part because of strain softening. Thus, the margins become inactive and preserve the features acquired  
 406 during the early stages of shearing while the active part gets progressively thinner (Fig. 15) and records the final stages  
 407 of shearing. The result is a shear zone with a deformation gradient toward the central part along which, as in the case of  
 408 the FMSZ, it is possible to observe variations in temperature, age of deformation and deformation regime (Fig. 13d).  
 409 The occurrence of allanite  $\pm$  apatite rims around monazites in mylonites is indicative of the breakdown of monazite  
 410 during retrograde metamorphism. Since allanite and apatite grew asymmetrically in extensional sites around the  
 411 monazite crystals, in agreement with the orientation of the instantaneous stretching axis during dextral shearing, it is  
 412 possible to state that this reaction took place synkinematically during retrograde metamorphism (Gibson et al., 2004)  
 413 and testify the further decrease in temperature during a late stage of shearing.

414 In the Alpine External Crystalline Massifs Variscan shear deformation has never been characterized in terms of  
 415 vorticity of the flow, and its age, considered to be between ~320 Ma and ~300 Ma (Bussy and Von Raumer, 1993;  
 416 Genier et al., 2008; Guillot et al., 2009) or Late Viséan (Musumeci and Colombo, 2002), was always inferred relying on  
 417 the age of emplacement of sin-kinematic granites. Ages of ~340 Ma obtained in this work are in agreement with the  
 418 age proposed by Musumeci and Colombo (2002). Ages of ~320 Ma are consistent with both magmatic ages present in  
 419 literature and ages of the dextral transpressional deformation in the Maures-Tanneron Massif (Schneider et al., 2014)  
 420 and Corsica-Sardinia (Carosi and Palmeri, 2002; Di Vincenzo et al., 2004; Iacopini et al., 2008), dated at ~320-310 Ma  
 421 (U-Th-Pb on monazites, Carosi et al., 2012), that affects migmatitic crust with strong tectono-metamorphic similarities  
 422 with the migmatites cropping out in the Argentera-Mercantour Massif. If we restore the counterclockwise Oligo-  
 423 Miocene rotation of the Corsica-Sardinia block (Vigliotti and Kent, 1990; Todesco and Vigliotti, 1993, Advokaat et al.,  
 424 2014) and of the Western Alps (Thomas et al., 1999; Collombet et al., 2002; Maffione et al., 2008), the three studied  
 425 sectors lie in lateral continuity and show a similar structural and metamorphic evolution. Shear deformation recognized  
 426 in northern Sardinia has been attributed to a network of dextral shear zones belonging to the East Variscan Shear Zone  
 427 (EVSZ; Corsini and Rolland, 2009; Carosi et al., 2012; Schneider et al., 2014). The FMSZ can be considered as a  
 428 branch of EVSZ. In the Argentera-Mercantour Massif dextral shear deformation started at ~340 Ma under amphibolite-  
 429 facies conditions. In the Maures-Tanneron Massif an anatectic post-collisional event is reported at ~340 Ma (Schneider  
 430 et al., 2014; Oliot et al., 2015) while in northern Sardinia collision-related MP - MT metamorphism has been recognized  
 431 at  $344 \pm 7$  Ma (Rb-Sr method; Ferrara et al., 1978), although older ages of the thickening stage also occur in Sardinia  
 432 and Corsica (between 380 and 340 Ma; Oliot et al., 2015). Although the different sectors of the southern European  
 433 Variscan Belt record a similar tectono-metamorphic evolution (Corsini and Rolland, 2009), the age of shearing along  
 434 the EVSZ is diachronous, and this is the first time that an age of ~340 Ma is obtained for amphibolite-facies mylonitic

435 deformation linked to this regional-scale system of shear zones. The different sectors of the belt are affected by orogen  
436 parallel dextral transpression (Carosi and Palmeri, 2002) at different time because of the progressive change of  
437 orientation of the belt with respect to the regional stress field (Carosi et al., 2012). This is also confirmed by the  
438 increase of the simple shear component of the deformation recognized both in Sardinia (Carosi and Palmeri, 2002), and,  
439 for the first time, in the Argentera-Mercantour Massif. Our data are therefore in agreement with the occurrence of a  
440 shear belt in the eastern sector of the Variscan Belt (Fig. 16).

441 Our new structural data support the model proposed by Rollet et al. (2002), Rosenbaum et al. (2002) and Advokaat et  
442 al. (2014) of the Corsica-Sardinia Block connected to southern France and in continuity with the Western Alps since all  
443 these sectors of the Variscan Belt show structural and lithological similarities, in contrast to reconstructions of the  
444 Variscan framework which show Corsica and/or Sardinia in a more westerly position connected to Spain (e.g., Fig. 8 in  
445 von Raumer et al., 2013).

446 In the western sector of the Iberian Massif, syn-anatectic sinistral transpressive deformation is recognized and dated at  
447 ~340 Ma using monazite and zircon (Pereira et al., 2008; 2010), therefore contemporary with the onset of shear  
448 deformation in the External Crystalline Massifs. Shearing in this sector of the belt is interpreted to be due to the  
449 formation of the Ibero-Armorican Arc. The presence of a contemporary system of shear zones with opposite kinematics  
450 in the western and eastern sector of the belt suggests that, as proposed by Matte (1986a,b), Garcia-Navarro and  
451 Fernandez (2004) and Pereira et al. (2008), the European Variscan Belt formed and evolved in a manner analogous to  
452 the indentation model proposed by Tapponier and Molnar (1977) and Tapponier et al. (1982). Our data are in agreement  
453 with a composite orocline model already proposed by Matte (1986a,b, 2001), Corsini and Rolland (2009), Guillot et al.  
454 (2009) and Carosi et al. (2012) with a western arc, still preserved, and an eastern arc that is truncated by the EVSZ.  
455 Our data support that the FMSZ is not a minor shear zone confined to one tectonic unit, but it is part of a large-scale  
456 system of shear zones that, because of its long-lasting activity, length and thickness, may have played a primary role in  
457 the exhumation of migmatitic rocks during Variscan time. Goscombe and Gray (2009) demonstrate that maximum  
458 stretching directions do not necessarily correlate with the flow vectors experienced during orogenesis. Although the  
459 stretching lineation in the FMSZ is shallowly inclined, the material flow may have had a large vertical component.

460

461

## 462 **7. Conclusive remarks**

463 The data obtained in this work allow us to establish that:



- 464 - the FMSZ is a dextral transpressional shear zone characterized by a non-coaxial flow with a component of pure shear  
465 and a component of simple shear, the latter increasing toward the central and most strained part of the shear zone;
- 466 - the FMSZ initiated during high-temperature amphibolite facies metamorphism and evidence of it is preserved in  
467 protomylonites and mylonites;
- 468 - Alpine deformation in the Argentera-Mercantour Massif occurred as local reactivation of Variscan structure and as  
469 localized reverse top-to-the-S shear zones, developed under greenschist facies conditions, cross-cutting the FMSZ  
470 mylonites;
- 471 - shear deformation started at ~ 340 Ma, near the metamorphic peak recorded in the GSV complex or shortly after it,  
472 and progressively migrated toward the core of the shear zone in a time span of ~10-20 Ma. In the same time interval a  
473 gradual change in the deformation regime is observed;
- 474 - microstructural and geochronological analysis constrain a type II evolution for this shear zone that can be a good  
475 example of strain softening within a regional-scale shear zone.
- 476 - the FMSZ is a sector of a system of regional-scale dextral shear zones occurring in the eastern sector of the Variscan  
477 Belt (EVSZ) at 320-310 Ma;
- 478 - shear deformation did not begin synchronously in all the part of the EVSZ but initiated earlier in its NE part and then  
479 propagated to the SW.

480

#### 481 **Software**

482 The data processing of the geochronological study was performed using the software GLITTER® (Macquarie Research  
483 Ltd 2001; Van Achterbergh et alii, 2001). The finite strain analysis was performed using the software EllipseFit 3.2 by  
484 Vollmer (2015). Calculation of the  $\theta$  angle was performed using the software Strain Calculator 3.2 by Holcombe  
485 (2009).

486

#### 487 **Acknowledgements**

488 Research supported by funds from Torino University (Ricerca Locale 2014, 2015), Pisa University (PRA 2016) and  
489 PRIN 2016 (prot. 2015EC9PJ5\_004; resp. R Carosi and C. Montomoli). We thank Michel Corsini and an anonymous  
490 reviewer for their careful revision that significantly improved the quality of the manuscript.

## 491 **References**

- 492 Advokaat E. L., van Hinsbergen D. J. J., Maffione M., Langereis C. G., Vissers R. L. M., Cherchi A., Schroeder R.,  
493 Madani H., Columbu S., 2014, Eocene rotation of Sardinia, and the paleogeography of the western Mediterranean  
494 region. *Earth Planet. Sci. Lett.*, 401, 183–195, doi:10.1016/j.epsl.2014.06.012.
- 495 Arthaud F., Matte P., 1977, Late Paleozoic strikeslip faulting in southern Europe and northern Africa: results of a right-  
496 lateral shear zone between the Appalachians and Urals. *Geological Society of America Bulletin*, 88, 1305–1320.
- 497 Baietto A., Perello P., Cadoppi P., Martinotti G., 2009, Alpine tectonic evolution and thermal water circulations of the  
498 Argentera Massif (South-Western Alps). *Swiss Journal of Geosciences* 102 (2), 223 - 245.
- 499 Ballèvre M., Bosse V., Ducassou C., Pitra P., 2009, Palaeozoic history of the Armorican Massif: models for the tectonic  
500 evolution of the suture zones. *Comptes Rendus Geoscience*, 341, 174–201.
- 501 Barale L., Bertok C., D’atri A., Martire L., Piana F., Domini G., 2016, Geology of the Entracque–Colle di Tenda area  
502 (Maritime Alps, NW Italy). *Journal of Maps*, 12, 359–370.
- 503 Bellot J.-P., 2005, The Palaeozoic evolution of the Maures massif (France) and its potential correlation with other areas  
504 of the Variscan belt: a review, in: Carosi R., Dias R., Iacopini D. & Rosenbaum G. (Eds.). *The southern Variscan belt*.  
505 *Journal of the Virtual Explorer, Electronic Edition*, ISSN, 19, 1441-8142.
- 506 Brun J.P, Burg J.P, 1982, Combined thrusting and wrenching in the Ibero-Armorican arc: A corner effect during  
507 continental collision. *Earth and Planetary Science Letters*, 61, 2, 319-332.
- 508 Burg J.-P., Matte P., 1978, A cross section through the French Massif Central and the scope of its Variscan  
509 Geodynamic Evolution. *Zeitschrift der Deutschen Geologischen Gesellschaft*, 129, 429–460.
- 510 Bussy F., Von Raumer J., 1993, U-Pb dating of Paleozoic events in the Mont Blanc Crystalline Massif, Western Alps.  
511 *Terra Abstract EUG07*, Strasbourg, 382-3.
- 512 Carosi R., Palmeri R., 2002, Orogen-parallel tectonic transport in the Variscan belt of northeastern Sardinia (Italy):  
513 implications for the exhumation of medium-pressure metamorphic rocks. *Geol. Mag.*, 139, 497 - 511.
- 514 Carosi R., Frassi C., Iacopini D., Montomoli C., 2005, Post-collisional transpressive tectonic in northern Sardinia. In:  
515 Carosi, R., Dias, R., Iacopini, D., Rosenbaum, G. (Eds.), *The Southern Variscan Belt*, Electronic Edition. *J. Virt. Expl.*  
516 1441-8142, vol. 19. Paper 4.
- 517 Carosi R., Montomoli C., Rubatto D., Visonà D., 2006, Normal-sense shear zones in the core of the Higher Himalayan  
518 Crystallines (Bhutan Himalayas): evidence for extrusion? In: LAW, R. D., SEARLE, M. P. & GODIN, L. (eds)  
519 *Channel Flow, Ductile Extrusion and Exhumation in Continental Collision Zones*. Geological Society, London, Special  
520 Publications, 268, 425-444.
- 521 Carosi R., Montomoli C., Visonà D., 2007, A structural transect in the Lower Dolpo: Insights on the tectonic evolution  
522 of western Nepal: *Journal of Asian Earth Sciences*, v. 29, p. 407-423.
- 523 Carosi R., Montomoli C., Rubatto D., Visonà D., 2010, Late Oligocene high-temperature shear zones in the core of the  
524 Higher Himalayan Crystallines (Lower Dolpo, western Nepal). *Tectonics*, 29, TC4029, doi: 10.1029/2008TC002400.

525 Carosi R., Montomoli C., Tiepolo M., Frassi C., 2012, Geochronological constraints on post-collisional shear zones in  
526 the Variscides of Sardinia (Italy), *Terra Nova*, 24, 42 - 51.

527 Carosi R., Montomoli C., Iaccarino S., Massonne H. J. Rubatto D., Langone A., Gemignani L., Visonà D., 2016a,  
528 Middle to late Eocene exhumation of the Greater Himalayan Sequence in the Central Himalayas: Progressive accretion  
529 from the Indian plate. *Geological Society of America Bulletin*, 128, 9 - 10, doi: 10.1130/B31471.1.

530 Carosi R., D’addario E., Mammoliti E., Montomoli C., Simonetti M., 2016b, Geological map of the northwestern  
531 portion of the Ferriere-Mollières shear zone, Argentera Massif, Italy. *Journal of Maps*, 12, 466-475.

532 Carrapa B., Wijbrans J., Bertotti G., 2003, Episodic exhumation in the Western Alps, *Geology*, 31, 7, 601– 604.

533 Challandes N., Marquer D., Villa I.M., 2003, Dating the evolution of C-S microstructures: a combined  $^{39}\text{Ar}$ - $^{40}\text{Ar}$  step-  
534 heating and UV laserprobe analysis of the Alpine Rofna shear zone. *Chemical Geology* 197 (1–4), 3–19.

535 Challandes N., Marquer D., Villa I., 2008, P–T-modelling, fluid circulation, and  $^{39}\text{Ar}$ - $^{40}\text{Ar}$  and Rb–Sr mica ages in the  
536 Aar Massif shear zones (Swiss Alps). *Swiss Journal of Geosciences* 101 (2), 269–288.

537 Collombet M., Thomas J. C., Chauvin A., Tricart P., Bouillin J. P., Gratier J. P., 2002, Counterclockwise rotation of the  
538 western Alps since the Oligocene: New insights from paleomagnetic data. *Tectonics*, 21, 4, 1032,  
539 doi:10.1029/2001TC901016.

540 Compagnoni R., Ferrando S., Lombardo B., Radulesco N., Rubatto D., 2010, Paleo-European crust of the Italian  
541 Western Alps: Geological history of the Argentera Massif and comparison with Mont Blanc-Aiguilles Rouges and  
542 Maures-Tanneron Massifs. In: (Eds.) M. Beltrando, A. Peccerillo, M. Mattei, S. Conticelli & C. Doglioni, *Journal of the*  
543 *Virtual Explorer*, volume 36, paper 4, doi: 10.3809/jvirtex.2009.00228

544 Corsini M., Ruffet G., Caby R., 2004, Alpine and late Hercynian geochronological constraints in the Argentera Massif  
545 (Western Alps). *Eclogae geologicae Helvetiae*, 97, 3 - 15.

546 Corsini M., Rolland Y., 2009, Late evolution of the southern European Variscan belt: exhumation of the lower crust in a  
547 context of oblique convergence. *Comptes Rendus Geosciences* 341 (2–3), 214–223.

548 Cottle J.M., Searle M.P., Jessup M.J., Crowley J.L., Law R.D., 2015, Rongbuk Re-visited: Geochronology of  
549 Leucogranites in the Footwall of the South Tibetan Detachment System, Everest Region, Southern Tibet. *Lithos*, 227,  
550 94 - 106.

551 Cruz M.J., Cunha J.C., Merlet C., Sabatè P., 1996, Datação pontual das monazitas da região de Itambé, Bahia, através  
552 da microsonda electronica XXXIX Congresso Brasileiro de Geologia, vol. 2, Sociedade Brasileira de Geologia-  
553 Núcleo, Bahia-Segipe, 206–209.

554 d’Atri A., Piana F., Barale L., Bertok C., Martire L., 2016, Geological setting of the southern termination of Western  
555 Alps. *Int J Earth Sci (Geol Rundsch)*, 105, 1831–1858. DOI 10.1007/s00531-015-1277-9.

556 Dias R., Ribeiro A., The Ibero-Armorican Arc: a collision effect against an irregular continent?. *Tectonophysics* 246,  
557 113-128.

558 Dias R., Ribeiro A., Romão J., Coke C., Moreira N., A review of the arcuate structures in the Iberian Variscides;  
559 constraints and genetic models. *Tectonophysics* 681, 170-194.

560 Di Vincenzo G., Carosi R., Palmeri R., 2004, The relationship between tectono-metamorphic evolution and argon  
561 isotope records in white mica: constraints from in situ  $^{40}\text{Ar}$ - $^{39}\text{Ar}$  laser analysis of the Variscan basement of Sardinia.  
562 *Journal of Petrology* 45, 5, 1013-1043.

563 Di Vincenzo G., Carosi R., Palmeri R., Tiepolo M., 2007, A comparative U-Th-Pb (zircon-monazite) and  $^{40}\text{Ar}$ - $^{39}\text{Ar}$   
564 (muscovite-biotite) study of shear zones in northern Victoria Land (Antarctica): Implications for geochronology and  
565 localized reworking of the Ross Orogen. *Journal of Metamorphic Geology*, 25, 605- 630.

566 Dunlap W., Teyssier C., McDougall I., Baldwin S., 1991, Ages of deformation from K/Ar and  $^{40}\text{Ar}/^{39}\text{Ar}$  dating of white  
567 micas. *Geology* 19, 1213–1216.

568 Erickson T.M., Pearce M.A., Taylor R.J.M., Timms N.E., Clark C., Reddy S.M., Buick I.S., 2015, Deformed monazite  
569 yields high-temperature tectonic ages: *Geology*, 43, 383–386, doi: 10.1130/G36533.1.

570 Faure-Muret A., 1955, Etudes géologiques sur le massif de l'Argentera-Mercantour et ses enveloppes sédimentaires.  
571 Mémoires pour servir à l'explication de la Carte géologique détaillée de la France, Paris, Imprimerie Nationale, France,  
572 with «Esquisse Géologique du Massif de l'Argentera-Mercantour et de sa Bordure Sédimentaire (Versant français) » at  
573 the 1/100.000 scale., pp 336.

574 Faure M., Lardeaux J. M., Ledru, P., 2009, A review of the pre-Permian geology of the Variscan French Massif Central.  
575 *Comptes Rendus Geosciences*, 341, 202–213.

576 Fernández-Lozano J., Pastor-Galán D., Gutiérrez-Alonso G., Franco P., New kinematic constraints on the Cantabrian  
577 orocline: A paleomagnetic study from the Peñalba and Truchas synclines, NW Spain. *Tectonophysics*, 681, 195–208.

578 Ferrara G., Ricci C. A., Rita F., 1978, Isotopic ages and tectono-metamorphic history of the metamorphic basement of  
579 north-eastern Sardinia. *Contributions to Mineralogy and Petrology* 68, 99 - 106.

580 Ferrando S., Lombardo B., Compagnoni R., 2008, Metamorphic history of HP mafic granulites from the Gesso-Stura  
581 Terrain (Argentera Massif, Western Alps, Italy). *European Journal of Mineralogy*, 20, 777 - 790.

582 Festa V., Prosser G., Caggianelli A., Grande A., Langone A., Mele D., 2016, Vorticity analysis of the Palmi shear zone  
583 mylonites: new insights for the Alpine tectonic evolution of the Calabria-Peloritani terrane (southern Italy). *Geological*  
584 *Journal* 51:670–681. doi: 10.1002/gj.2673.

585 Fluck P., Piqué A., Schneider J. L., Whitechurch H., 1991., Le socle vosgien. *Sciences Géologiques*, 44, 207–235.

586 Fossen H., Tikoff B., 1993, The deformation matrix for simultaneous simple shearing, pure shearing and volume  
587 change, and its application to transpression-transension tectonics. *Journal of Structural Geology*, 15, 413–422, DOI:  
588 10.1016/0191-8141(93)90137-Y.

589 Fossen H., Tikoff B., Teyssier C., 1994, Strain modeling of transpressional and transtensional deformation. *Norsk Geol.*  
590 *Tidsskr.* 74, 134–145.

591 Fossen H., 2016, *Structural Geology*. Cambridge University Press, p 510.

592 Fossen H., Cavalcante G. C. G., 2017, Shear zones – A review. *Earth-Science Reviews*, 171, 434–455.

593 Franke W., 1989, Tectonostratigraphic units in the Variscan belt of central Europe. In: Dallmeyer, R. D. (ed.) *Terranes*  
594 *in the Circum-Atlantic Paleozoic Orogens*. Geological Society of America Special Papers, 230, 67–90.

595 Franke W., Robin L. M. C., Torsvik T. H., 2017, The Palaeozoic Variscan Oceans Revisited. *Gondwana Research*, 48,  
596 257–284. doi: 10.1016/j.gr.2017.03.005.

597 Fry N., 1979, Random point distribution and strain measurement in rocks. *Tectonophysics*, 60, 89–105.

598 Garcia-Navarro E., Fernandez C., 2004, Final stages of the Variscan orogeny at the southern Iberian massif: Lateral  
599 extrusion and rotation of continental blocks. *Tectonics*, 23, tc6001, doi:10.1029/2004tc001646.

600 Gasquet D., Bertrand J.M., Paquette J.L., Lehmann J., Ratzoy G., De Ascensão Guedes R., Tiepolo M., Boullier A.M.,  
601 Scaillet S., Nomade S., 2010, Miocene to Messinian deformation and hydrothermal activity in a pre-Alpine basement  
602 massif of the French western Alps: new U–Th–Pb and argon ages from the Lauzière massif. *Bulletin de la Société*  
603 *Géologique de France*, 181, 227–241.

604 Genier F., Epard J.L., 2007, the Fry method applied to an augen orthogneiss: problems and results. *Journal of structural*  
605 *geology*, 29, 209–244.

606 Genier F., Bussy F., Epard J.L., Baumgartner L., 2008, Water-assisted migmatization of metagraywackes in a Variscan  
607 shear zone, Aiguilles-Rouges Massif, western Alps: *Lithos*, v. 102, p. 575–597.

608 Gibson H.D., Carr S.C., Brown R.L., Hamilton M.A., 2004, Correlations between chemical and age domains in  
609 monazite, and metamorphic reactions involving major pelitic phases: an integration of ID-TIMS and SHRIMP  
610 geochronology with Y–Th–U X-ray mapping. *Chemical Geology*, 211, 237–260.

611 Gillam B. G., Little T. A., Smith E., Toy V. G., 2013, Extensional shear band development on the outer margin of the  
612 Alpine mylonite zone, Tatare Stream, Southern Alps, New Zealand. *Journal of Structural Geology*, 54, 1–20.

613 Goscombe B. D., Hand M., Gray D., Mawby J., 2003, The metamorphic architecture of a transpressional orogen: The  
614 Kaoko Belt, Namibia. *J. Pet.* 44, 679–711.

615 Goscombe B., David G., Richard A., David A. F., James V., 2005, Event geochronology of the Pan-African Kaoko  
616 Belt, Namibia. *Precambrian Research*, 140, 103.e1–103.e41.

617 Goscombe B. D., Grey D. R., 2009, Metamorphic response in orogens of different obliquity, scale and geometry.  
618 *Gondwana Research*, 15, 2, 151–167.

619 Guillot S., Ménot R.P., 2009, Paleozoic evolution of the External Crystalline Massifs of the Western Alps. *C.R.*  
620 *Geosciences*, 341, 253–265.

621 Guillot S., Di Pola S., Ménot R. P., Ledru P., Spalla M. I., Gosso G., Schwartz S., 2009, Suture zone and importance of  
622 strike-slip faulting for Variscan geodynamic reconstructions of the External Crystalline Massifs of the Western Alps.  
623 *Bulletin de la Société Géologique de France*, 180, 6, 483–500.

624 Holcombe R., 2009, RJH StrainCalculator 3.2.

625 Horstwood M.S.A., Foster G.L., Parrish R.R., Noble S.R., Nowell G.M., 2003, Common-Pb corrected in situ U-Pb  
626 accessory mineral geochronology by LA-MCICP-MS: *Journal of Analytical Atomic Spectrometry*, 18, 837–846.

627 Hudleston P., 1999, Strain compatibility and shear zones: is there a problem? *Journal of Structural Geology*, 21, 923–  
628 932.

629 Iaccarino S., Montomoli C., Carosi R., Massonne H.-J., Langone A., Visonà D., 2015, Pressure-temperature-time-  
630 deformation path of kyanite-bearing migmatitic paragneiss in the Kali Gandaki valley (central Nepal): Investigation of  
631 late Eocene–early Oligocene melting processes: *Lithos*, v. 231, p. 103–121, doi: 10.1016 /j .lithos .2015.06 .005 .

632 Iaccarino S., Montomoli C., Carosi R., Massonne H.-J., Visonà D., 2017, Geology and tectono-metamorphic evolution  
633 of the Himalayan metamorphic core: insights from the Mugu Karnali transect, Western Nepal (Central Himalaya).  
634 *Journal of Metamorphic Geology*, 35, 3, 301–325.

635 Iacopini D., Carosi R., Montomoli C., Passchier C. W., 2008, Strain analysis of flow in the Northern Sardinian  
636 Variscan Belt: recognition of a partitioned oblique deformation event. *Tectonophysics*, 221, 345 - 359.

637 Iacopini D., Carosi R., Xypolias P., 2010, Implications of complex eigenvalues in homogeneous flow: a three-  
638 dimensional kinematic analysis. *Journal of Structural Geology*, 32, 1, 93–106.

639 Iacopini D., Frassi C., Carosi R., Montomoli C., 2011, Limits and biases on the three-dimensional vorticity analysis  
640 using porphyroblast system: a discussion and application to natural example, In: *Deformation Mechanism, Rheology &*  
641 *Tectonics: Microstructures, Mechanics & Anisotropy*, Special issue, 2011, Special Publication - Geological Society of  
642 London, 360, 301–318.

643 Kohn M. J., Wiernad M., Parkinson C. D., Upreti B. N., 2005, Five generations of monazite in Langtang gneisses:  
644 Implication for chronology of the Himalayan metamorphic core. *Journal of Metamorphic Geology*, 23, 399 - 406.

645 Kohn M.J., 2008, P-T-t data from Nepal support critical taper and repudiate large channel flow of the Greater  
646 Himalayan Sequence: Geological Society of America Bulletin, 120, 259–273.

647 Kurz G.A., Northrup C.J., 2008, Structural analysis of mylonitic fault rocks in the Cougar Creek Complex,  
648 OregonIdaho using the porphyroclast hyperbolic distribution method, and potential use of SC'-type extensional shear  
649 bands as quantitative vorticity indicators. Journal of Structural Geology 30, 1005-1012.

650 Larson K. P., Cottle M. J., 2015, Initiation of crustal shortening in the Himalaya. Terra Nova, 27, 169 - 174.

651 Larson K.P., Godin L., 2009, Kinematics of the Greater Himalayan Sequence, Dhaulagiri Himal: Implications for the  
652 structural framework of central Nepal: Journal of the Geological Society, 166, 25-43.

653 Law R. D., Searle M. P., Simpson R. L., 2004, Strain, deformation temperatures and vorticity of flow at the top of the  
654 Greater Himalayan Slab, Everest Massif, Tibet. Journal of the Geological Society, London, 161, 305-320

655 Li P., Sun M., Rosenbaum G., Cai K., Chen M., He Y., 2016, Transpressional deformation, strain partitioning and fold  
656 superimposition in the southern Chinese Altai, Central Asian Orogenic Belt (Article). Journal of Structural Geology,  
657 87, 64-80.

658 Ludwig K.R., 2003, Isoplot/Ex Version 3.0: A Geochronological Toolkit for Microsoft Excel: Berkeley Geochronology  
659 Center Special Publication, 4, 74 pp.

660 Maffione M., Speranza F., Faccenna C., Cascella A., Vignaroli G., Sagnotti L., 2008, A synchronous Alpine and  
661 Corsica-Sardinia rotation. J. Geophys. Res., 113, B3, doi:10.1029/2007JB005214.

662 Malaroda R., Carraro F., Dal Piaz G. V., Franceschetti B., Sturani C., Zanella E., 1970, Carta geologica del Massiccio  
663 dell'Argentera alla scala 1:50.000 e note illustrative. Memorie della Società Geologica Italiana. Volume 9, 557 - 663.

664 Matte P., Ribeiro A., 1975, Forme et orientation de l'ellipsoïde de déformation dans la virgation hercynienne de Galice.  
665 Relations avec le plissement et hypothèses sur la genèse de l'arc ibéro-armoricain. CR Acad. Sci. Paris, 280, 2825–  
666 2828.

667 Matte P., 1986a, La Chaîne varisque parmi les chaînes paléozoïques péri-atlantiques, modèle d'évolution et position des  
668 grands blocs continentaux au Permo-Carbonifère. Bull. Soc. Geol. France 8, 4 - 24.

669 Matte, P., 1986b. Tectonics and plate tectonics model for the Variscan belt of Europe. Tectonophysics, 126, 329 - 374.

670 Matte, P., 2001, The Variscan collage and orogeny (480–290 Ma) and the tectonic definition of the Armorica  
671 microplate: a review: *Terra nova*, 13, p. 122–128.

672 Monié P., Maluski H., 1983, Données géochronologiques <sup>39</sup>Ar/<sup>40</sup>Ar sur le socle ante Permien du massif de l'Argentera-  
673 Mercantour (Alpes-Maritimes, France). Bull. Soc. Géol. France 7, 247–257.

674 Montomoli C., Iaccarino S., Carosi R., Langone A., Visonà D., 2013, Tectonometamorphic discontinuities within the  
675 Greater Himalayan Sequence in western Nepal (central Himalaya): Insights on the exhumation of crystalline rocks.  
676 Tectonophysics, 608, 1349 - 1370.

677 Montomoli C., Carosi R., Iaccarino S., 2015, Tectonometamorphic discontinuities in the Greater Himalayan Sequence:  
678 A local or a regional feature? In Mukherjee, S., Carosi, R., van der Beek, P.A., Mukherjee, B.K., and Robinson, D.M.,  
679 eds., Tectonics of the Himalaya: Geological Society of London Special Publication 412, 25 - 41, doi: 10 .1144 /SP412  
680 .3.

681 Mulch A., Cosca M.A., 2004. Recrystallization or cooling ages: in situ UV-laser <sup>40</sup>Ar/<sup>39</sup>Ar geochronology of muscovite  
682 in mylonitic rocks. Journal of the Geological Society, London 161 (4), 573–582.

683 Musumeci G., Colombo F., 2002, Late Visean mylonitic granitoids in the Argentera Massif (Western Alps): age and  
684 kinematic constraints on the Ferrière-Mollières shear zone. *Comptes Rendus de l'Académie des Sciences Serie II* 334,  
685 213 - 220.

686 Nabavi S. T., Diaz-Azpiroz M., Talbot C.J., 2016, Inclined transpression in the Neka Valley, eastern Alborz, Iran. *Int J*  
687 *Earth Sci (Geol Rundsch)*, doi: 10.1007/s00531-016-1388-y.

688 Oliot, E., Melleton, J., Schneider, J., Corsini, M., Gardien, V. and Rolland, Y., 2015. Variscan crustal thickening in the  
689 Maures-Tanneron massif (South Variscan belt, France): new in situ monazite U-Th-Pb chemical dating of high-grade  
690 rocks: *Bulletin de la Société géologique de France*, 186, p. 145–169, doi: 10.2113/gssgfbull.186.2-3.145.

691 Padovano M., Elter F. M., Pandeli E., Franceschelli M., 2012, The East Variscan Shear Zone: new insights into its role  
692 in the Late Carboniferous collision in southern Europe. *International Geology Review*, 54, 957–970.

693 Padovano M., Dörr W., Elter F. M., Gerdes A., 2014, The East Variscan Shear Zone: Geochronological constraints  
694 from the Capo Ferro area (NE Sardinia, Italy). *Lithos*, 196-197, 27-41.

695 Paquette J.L., Tiepolo M., 2007. High resolution (5  $\mu$ m) U–Th–Pb isotope dating of monazite with excimer laser  
696 ablation (ELA)–ICPMS. *Chemical Geology*, 240, 222–237.

697 Passchier C.W., 1987, Stable position of rigid objects in non-coaxial flow: a study in vorticity analysis. *Journal of*  
698 *Structural Geology*, 9, n° 5/6, pp 679-690.

699 Passchier C.W., 1991, The classification of dilatant flow type. *Journal of Structural Geology*, 13, 101-104.

700 Passchier C.W., Trouw R.A.J., 2005, *Microtectonics*, Springer-Verlag Berlin Heidelberg, p 101.

701 Pereira M.F., Arturo Apraiz A., Silva J.B., Chichorro M., 2008, Tectonothermal analysis of high-temperature  
702 mylonitization in the Coimbra–Córdoba shear zone (SW Iberian Massif, Ouguela tectonic unit, Portugal): evidence of  
703 intra-continental transcurrent transport during the amalgamation of Pangea. *Tectonophysics* 461, 378–394.

704 Pereira M.F., Silva J.B., Drost K., Chichorro M., Apraiz A., 2010,. Relative timing of transcurrent displacements in  
705 northern Gondwana: New U–Pb laser ablation MS–ICP–MS zircon and monazite geochronology of gneisses and  
706 sheared granites from the Western Iberian Massif (Portugal). *Gondwana Research* 17 (2–3), 461–481.

707 Piazzolo S., Passchier C. W., 2002, experimental modelling of viscous inclusions in a circular high-strain ring:  
708 implication for the interpretation of shape fabrics and deformed enclaves. *J Geophy Res*, 107, B10, 2242, ETG 11: 1 -  
709 15.

710 Platt J., Vissers R., 1980, Extensional structures in anisotropic rocks. *Journal of Structural Geology* 2, 397-410.

711 Pyle J. M., Spear F. S., 1999, Yttrium zoning in garnet: coupling of major and accessory phases during metamorphic  
712 reactions. *Geol. Mat. Res.* 1, 1 - 49

713 Pyle J. M., Spear F. S., Rudnick R. L., Mcdonough W. F., 2001, Monazite-xenotime-garnet equilibrium in metapelites  
714 and a new monazite-garnet thermometer. *J. Petrol.*, 42, 2083–10.

715 Rolin P., Marquer D., Colchen M., Cartannaz C., Cocherie A., Thierry V., Quenardel J. M., Rossi P., 2009, Famenco-  
716 Carboniferous (370-320 Ma) strike slip tectonics monitored by syn-kinematic plutons in the French Variscan belt  
717 (Massif Armoricaín and French Massif Central). *Bull. Soc. Géol. Fr.*, 180, 3, 231-246.

718 Rollet N., Déverchère J., Beslier M.-O., Guennoc P., Réhault J.-P., Sosson M., Truffert C., 2002, Back arc extension,  
719 tectonic inheritance, and volcanism in the Ligurian Sea, Western Mediterranean: Ligurian Sea Back Arc structure and  
720 evolution, *Tectonics*, 21, 3, 6-1-6–23, doi:10.1029/2001TC900027.

- 721 Rubatto D., Schaltegger U., Lombardo B., Colombo F., Compagnoni R., 2001, Complex Paleozoic magmatic and  
722 metamorphic evolution in the Argentera Massif (Western Alps) resolved with U–Pb dating. *Schweizerische*  
723 *mineralogische und petrographische Mitteilungen*, 81, 213–228.
- 724 Sanchez G., Rolland Y., Schreiber D., Giannerini G., Corsini M., Lardeaux, J.-M., 2010, The active fault system of SW  
725 Alps. *J. Geodyn.*, 49, 296–302.
- 726 Sanchez G., Rolland Y., Schneider J., Corsini M., Oliot E., Goncalves P., Verati C., Lardeaux J.M., Marquer D., 2011,  
727 Dating low-temperature deformation by  $^{40}\text{Ar}/^{39}\text{Ar}$  on white mica, insights from the Argentera-Mercantour Massif (SW  
728 Alps). *Lithos* 125, 521 - 536.
- 729 Sarkarinejad K., Azizi A., 2008, Slip partitioning and inclined dextral transpression along the Zagros Thrust System,  
730 Iran. *J Struct Geol*, 30, 116-136.
- 731 Sarkarinejad K., Keshavarz S., Faghih A., 2015, Kinematics of the Sirjan mylonite nappe, Zagros Orogenic Belt:  
732 insights from strain and vorticity analyses. *Journal of Geosciences*, 60, 189-202.
- 733 Schneider J., Corsini M., Reverso-Peila A., Lardeaux J. M., 2014, Thermal and mechanical evolution of an orogenic  
734 wedge during Variscan collision: an example in the Maures-Tanneron massif (SE France). *Geol. Soc., London, spec.*  
735 *publ.*, 405, 313-331.
- 736 Seydoux-Guillaume A.M., Paquette J.L., Wiedenbeck M., Montel J.M., Heinrich W., 2002a, Experimental resetting of  
737 the U–Th–Pb system in monazite. *Chemical Geology*, 191, 165–181.
- 738 Seydoux-Guillaume A.M., Wirth R., Nasdala L., Gottschalk M., Montel J.M., Heinrich W., 2002b, XRD, TEM and  
739 Raman study of experimental annealing of natural monazite. *Physics and Chemistry of Minerals*, 29, 240–253.
- 740 Simonetti M., Carosi R., Montomoli C., 2017, Variscan shear deformation in the Argentera Massif: a field guide to the  
741 excursion in the Ponteb Bernardo Valley (CN, Italy). *Atti della Società Toscana di Scienze Naturali Memorie, Serie A*,  
742 124, doi: 10.2424/ASTSN.M.2017.02.
- 743 Simpson C., De Paor D.G., 1993, Strain and kinematic analysis in general shear zones. *Journal of Structural Geology*.  
744 15, 1-20.
- 745 Skrzypek E., Stipskà, P., Cocherie A., 2012, The origin of zircon and the significance of U–Pb ages in high-grade  
746 metamorphic rocks: a case study from the Variscan orogenic root (Vosges Mountains, NE France). *Contributions to*  
747 *Mineralogy and Petrology*, 164, 935–957.
- 748 Stampfli G.M., von Raumer L.F., Borel G.D., 2002, Paleozoic evolution of pre-Variscan terranes: from Gondwana to  
749 the Variscan collision. *Geol. S. Am. S.*, 364, 263-280.
- 750 Tapponnier P., Molnar P.J., 1977, Active faulting and tectonics in China. *J. Geophys. Res.* 82, 2905–2930.
- 751 Tapponnier P., Peltzer G., Le Dain A.Y., Armijo R., Cobbold P., 1982, Propagating extrusion tectonics in Asia: new  
752 insights from simple experiments with plasticine. *Geology* 10, 611–616.
- 753 Thomas J. C., Claudel M. E., Collombet M., Tricart P., Chauvin A., Dumont T., 1999, First paleomagnetic data from  
754 the sedimentary cover of the French penninic Alps: Evidence for Tertiary counterclockwise rotations in the western  
755 Alps. *Earth Planet. Sci. Lett.*, 171, 561–574.
- 756 Thompson, A.B., Schulmann, K., Jezek, J., 1997, Thermal evolution and exhumation in obliquely convergent  
757 (transpressive) orogens. *Tectonophysics*, 280, 171-184.
- 758 Tiepolo M., 2003, In situ Pb geochronology of zircon with laser ablation–inductively coupled plasma-sector field mass  
759 spectrometry. *Chemical Geology*, 199, 159–177.
- 760 Todesco M., Vigliotti L., 1993, When did Sardinia rotate? Statistical evaluation of the paleomagnetic data. *Annali di*  
761 *Geofisica*, Vol. 30, N. 5 – 6.



- 762 Tollmann A., 1982, Großraumiger variszischer Deckenbau im Moldanubikum und neue Gedanken zum Variszikum  
763 Europas. Geotektonische Forschungen, 64, 1–91.
- 764 Turco E., Macchiavelli C., Mazzoli S., Schettino A., Pierantoni P.P., 2012, Kinematic evolution of Alpine Corsica in  
765 the framework of Mediterranean mountain belts. Tectonophysics, 579, 193-206.
- 766 Van Achterbergh E., Ryan C. G., Jackson S. E., Griffin W., 2001, Data reduction software for LA-ICP-MS. In:  
767 Sylvester, P. (Ed.), Laser Ablation ICPMS in the Earth Sciences. Mineralogical Association of Canada, Short Course  
768 Series, 29, 239 - 243.
- 769 Vigliotti L., Kent D.V., 1990, Paleomagnetic results of Tertiary sediments from Corsica: evidence of post-Eocene  
770 rotation. Phys. Earth Planet. Inter., 62, 97 - 108.
- 771 Villa I.M., Ruggieri G., Puxeddu M., 1997, Petrological and geochronological discrimination of two white-mica  
772 generations in a granite cored from the Larderello-Travale geothermal field (Italy). European Journal of Mineralogy 9,  
773 563–568.
- 774 Villa I. M., Bucher S., Bousquet R., Kleinhanns T. C., Schmid S. M. 2014, Dating polygenic metamorphic assemblages  
775 along a transect across the the western Alps. Journal of Petrology, 55 (4), 803-830.
- 776 Villa I. M., 2015, <sup>39</sup>AR-<sup>40</sup>AR geochronology of mono- and polymetamorphic basement rocks, Periodico di Mineralogia,  
777 84 (3B), 615-632.
- 778 Vollmer f. W., 2015, EllipseFit 3 user manual, pp. 72.
- 779 von Raumer J. F., Bussy F., Schaltegger U., Schulz B., Stampfli G. M., 2013, Pre-Mesozoic Alpine basements—Their  
780 place in the European Paleozoic framework. Geol. Soc. Am. Bull., 125, 1–2, 89–108, doi:10.1130/B30654.1.
- 781 Wallis S. R., Platt J. P., Knott S. D., 1993, Recognition of syn-convergence extension in accretionary wedges with  
782 examples from Calabrian arc and the Eastern Alps. American Journal of Sciences ,293, 463-495.
- 783 Williams M. L., Jercinovic M.J., Hetherington C. J., 2007, Microprobe Monazite Geochronology: Understanding  
784 Geologic Processes by Integrating Composition and Chronology. Annual Review of Earth Planetary Sciences, 35, 137 -  
785 75.
- 786 Wu W., Liu J., Zhang L., Qi Y., Ling C., 2016, Characterizing a middle to upper crustal shear zone: microstructures,  
787 quartz c-axis fabrics, deformation temperatures and flow vorticity analysis of the northern Ailao Shan-Red River shear  
788 zone. Journal of Asian Earth Sciences.
- 789 Xypolias P., Kokkalas S., 2006, Heterogeneous ductile deformation along a midcrustal extruding shear zone: an  
790 example from the External Hellenides (Greece). In: Law, R.D., Searle, M.P., Godin, L. (Eds.), Channel Flow, Ductile  
791 Extrusion, and Exhumation in Continental Collision Zones. Geological Society, London, Special Publications, 268,  
792 497-516.
- 793 Xypolias P., 2010, Vorticity analysis in shear zones: A review of methods and applications. Journal of Structural  
794 Geology, 32, 2072 – 2092.
- 795 Zhang Q., Teyssier C., 2013, Flow vorticity in Zhangbaling transpressional attachment zone, SE China. Journal of  
796 Structural Geology, 48, 72-84.

797

## 798 **Figure captions**

799 **Figure 1.** A) Distribution of the Variscan units in Europe at the present day. S = Sardinia; C = Corsica; MTM =  
800 Maures-Tanneron Massif; MC = Massif Central; IM = Iberian Massif; AM = Armorican Massif; RH= Rheno-  
801 Hercynian; BM = Bohemian Massif; V = Vosges. Blue circle indicates the location of the Argentera Massif (modified

802 after Compagnoni et al., 2010); B) Geological sketch map of the Argentera-Mercantour Massif. FMSZ: Ferriere-  
 803 Mollières shear zone; FCSZ: Fremamorta-Colle del Sabbione shear zone; BF: Bersezio fault; VLS: Valle Stura  
 804 Leucogranite; ACG: Argentera Central Granite (modified after Compagnoni et al., 2010).

805 **Figure 2.** Geological map of the northwestern portion of the Ferriere-Mollières shear zone (modified after Carosi et al.,  
 806 2016b). Rectangles indicate sampling areas: transect A; transect B; transect C. Details of the selected areas are shown in  
 807 figure 6 and cross sections are shown in figure 14. Equal angle, lower hemisphere projections are also shown: 1)  
 808 Mineral lineation (red), poles to mylonitic foliation (black) and poles to ultramylonitic foliation (yellow triangles) in  
 809 mylonitic schist with biotite and white mica. 2) Mineral lineation (red) and poles to mylonitic foliation (black) in  
 810 mylonitic gneiss with biotite and white mica. 3) Axial plane poles (blue) and axes (red) of the post-shearing folds. 4)  
 811 Lineation (red) and mylonitic foliation poles (black) in the alpine shear zones.

812 **Figure 3.** A) protomylonites at the outcrop-scale; B) anastomosing disjunctive cleavage in protomylonites. It is possible  
 813 to recognize K-feldspar, plagioclase and quartz in a medium grained biotite and sillimanite matrix with some white  
 814 mica (plane-polarized light); C) mylonites at the outcrop-scale; D) disjunctive cleavage with sub-parallel cleavage  
 815 domains in mylonites. Quartz, K-feldspar and plagioclase porphyroclasts in a fine grained biotite and white mica matrix  
 816 are recognizable (plane-polarized light); E) ultramylonites at the outcrop-scale; F) continuous cleavage marked by white  
 817 mica and chlorite in ultramylonites (plane-polarized light).

818 **Figure 4.** Micrographs (crossed polars) of the kinematic indicators showing a top-to-the-SE sense of shear in the  
 819 FMSZ. The short and the long borders of each micrograph are parallel to the Z and X axes of the strain ellipsoid,  
 820 respectively. A) white mica fish and S-C' fabric; B) K-feldspar  $\sigma$ -type porphyroclast (yellow), C' plane (green) and  
 821 oblique foliation (orange) in quartz level; C) S-C' fabric. D) Subgrain rotation and recrystallization in quartz (crossed  
 822 polars); E) Undulose extinction in K-feldspar porphyroclasts (crossed polars).

823 **Figure 5.** Low-angle Alpine shear zones. A) S-C fabric at the outcrop scale; B) S-C and S-C' fabric in thin section  
 824 (plane-polarized light); C) Deformed foliation with biotite relicts (plane-polarized light). The short and the long borders  
 825 of each micrograph are parallel to the Z and X axes of the strain ellipsoid, respectively. All kinematic indicators show a  
 826 reverse top-to-the-S sense of shear.

827 **Figure 6.** Detailed geological maps of the three studied transects along which samples were collected: A) transect A; B)  
 828 transect B; C) transect C. Samples used for kinematic vorticity and strain analysis are indicated with red stars, whereas  
 829 samples used for the geochronological study are indicated with yellow stars. Legend as in Figure 1.

830  
 831 **Figure 7.** A) To the right, micrograph (crossed polars) showing C' planes in mylonite of the FMSZ (the short and the  
 832 long borders of the micrograph are parallel to Z and X axes of the finite strain ellipsoid, respectively). To the left,  
 833 schematic diagram of possible microstructures developed under general flow conditions in a mylonite with dextral  
 834 sense of shear and their appearance in thin section. The flow apophyses A1 and A2 are indicated in red and green,  
 835 respectively. The angle  $2v$  between the two apophyses (yellow) is bisected by the C' shear plane (dotted line). The  
 836 equation to calculate  $W_k$  is also shown (modified after Kurz and Northrup, 2008). B) Relation to calculate the  
 837 shortening value S perpendicular to the flow plane on the basis of the values of both the mean kinematic vorticity  
 838 number  $W_m$ , that can be assumed equal to  $W_k$ , and the axial ratio of the strain ellipse measured on the XZ section  
 839 (modified after Law et al., 2004).

840 **Figure 8.** Polar histograms used to derive the angle  $v$  and to calculate kinematic vorticity with the S-C' method (Kurz  
 841 and Northrup, 2008) on field oriented samples. A1 = flow apophysis 1; A2 = flow apophysis 2. Dashed line represent  
 842 the bisector of the angle between A1 and A2, green bars represent the number of data. All histograms are shown with  
 843 the same sense of shear (red arrows).

844  
 845 **Figure 9.** Fry graphs used in the strain analysis obtained with the center-to-center method on the XZ sections; n =  
 846 number of centers used for the Fry analysis. A) ARG 143; B) ARG 144; C) ARG 21a; D) ARG 68; E) ARG 117; F)  
 847 ARG 19; G) ARG 21; H) ARG 27; I) ARG 29. Axial ratios  $R_{xz}$  are reported in table 1.

848  
 849 **Figure 10.** Back-scattered electron pictures of monazite grains in different microstructural position: A) Mnz 59, sample  
 850 ARG 48b, included in garnet; B) Mnz 29, sample ARG 29, included in a white mica fish; C) Monazite with asymmetric

851 shape along the main foliation marked by biotite in protomylonite (Mnz 14, sample ARG19); D) Monazite along the  
852 main foliation in mylonite (Mnz 52, sample ARG 27).

853 **Figure 11.** Back-scattered electron images of the analyzed monazites and related compositional maps of Y made by  
854 electron microprobe. Red dots represent the spots of the quantitative chemical analyses (data are reported in Online  
855 Resource 1).

856  
857 **Figure 12.** Distribution of  $^{206}\text{Pb}/^{238}\text{U}$  (A) and  $^{208}\text{Pb}/^{232}\text{Th}$  (B) ages for different samples along the deformation  
858 gradient. Black vertical bars indicate concordant ages, black horizontal bar contains the averaged data (MSWD=Mean  
859 Square Weighted Deviates; prob.= probability). Geochronological data define a broad trend (grey area) reflecting the  
860 deformation degree.

861  
862 **Figure 13.** A) Percentage of pure shear (PS) and simple shear (SS) in relation to the calculated maximum and minimum  
863 Wk values; B) simplified sketch showing orientation of the instantaneous flow elements and their angular relationships  
864 in a dextral shear zone with simultaneous pure shear and simple shear,  $\theta$  is the angle between  $\text{ISA}_{\text{max}}$  and the shear zone  
865 boundary (modified after Xypolias, 2010); C) diagram showing relationship between the orientation of the maximum  
866 Instantaneous Stretching Axis ( $\text{ISA}_{\text{max}}$ ) with respect to the shear zone boundary (angle  $\theta$ ) related to the kinematic  
867 vorticity number Wk (modified after Fossen and Tikoff, 1993; Fossen et al., 1994) Wk value for which simple shear =  
868 pure shear is 0,71 according to Law et al., 2004 and Xypolias, 2010. The distribution of the samples shows a variation  
869 from a pure shear dominated transpression to a simple shear dominated transpression linked to the increase of the  
870 vorticity number. Orange dashed line represents the theoretical trend of the angle  $\theta$ . It is possible to observe that the  
871 distribution of the values of angle  $\theta$  of the studied samples is in good agreement with the theoretical curve; D) variation  
872 of the vorticity number in relation with the distance of the sample from the center of the shear zone. The distribution of  
873 points shows increasing Wk values (i.e. increasing of simple shear component of deformation) toward the central part  
874 of the shear zone (trend: blue dashed line).

875 **Figure 14.** Parallel cross sections along the deformation gradient (modified after Carosi et al., 2016b). The position of  
876 the analyzed samples and the relative  $^{206}\text{Pb}/^{238}\text{U}$  (red) and  $^{208}\text{Pb}/^{232}\text{Th}$  (blue) ages are reported. Traces of the geological  
877 cross sections and the legend are reported in figure 2.

878 **Figure 15.** Evolution of the Ferriere-Mollières Shear Zone according to a type II growth model (Fossen, 2010) and  
879 relationship between deformation gradient and age of shear deformation: the margins become progressively inactive  
880 and preserve the features acquired during the older stages of shearing while the active part gets progressively thinner  
881 and records the younger stages of shear zone activity.

882 **Figure 16.** Reconstruction of the Variscan Belt during Permian (modified after Guillot and Ménot, 2009; Carosi et al.,  
883 2012). Age of shearing in the eastern sector of the Variscan Belt are reported. The East Variscan Shear Zone (EVSZ)  
884 affects the Argentera-Mercantour Massif (AR) at ~ 340 Ma and then propagated southward affecting the Maures-  
885 Tanneron Massif (MTM) and Corsica and Sardinia (SA) at ~ 320 Ma (Carosi et al., 2012). BM = Bohemian Massif.  
886

887 **Table 1.** Kinematic vorticity numbers obtained by the S-C' method and strain data of samples from the three transects.  
888 N = number of C' plane;  $v_{\text{max}}$  = measured maximum angle between C' plane and S plane;  $2v$  = calculated angle  
889 between apophysis A1 and apophysis A2; Wk = vorticity number; Angle  $\theta$  = angle between the  $\text{ISA}_{\text{max}}$  and the shear  
890 zone boundary; n = number of centers used for the Fry analysis. Shortening and Stretching values, deformation and  
891 position of the sample are also reported.

892 **Table 2.** Standards analyzed for the geochronological study at the beginning and at the end of each run.

893 **Table 3.** Geochronological data obtained from the monazites of the samples ARG 19, ARG 21, ARG 27, ARG 29 and  
894 ARG 48b.

895 **Online Resource 1.** Chemical quantitative analyses of the monazites of the sample ARG 19, ARG 21, ARG 27, ARG  
896 29 and ARG 48b.

897

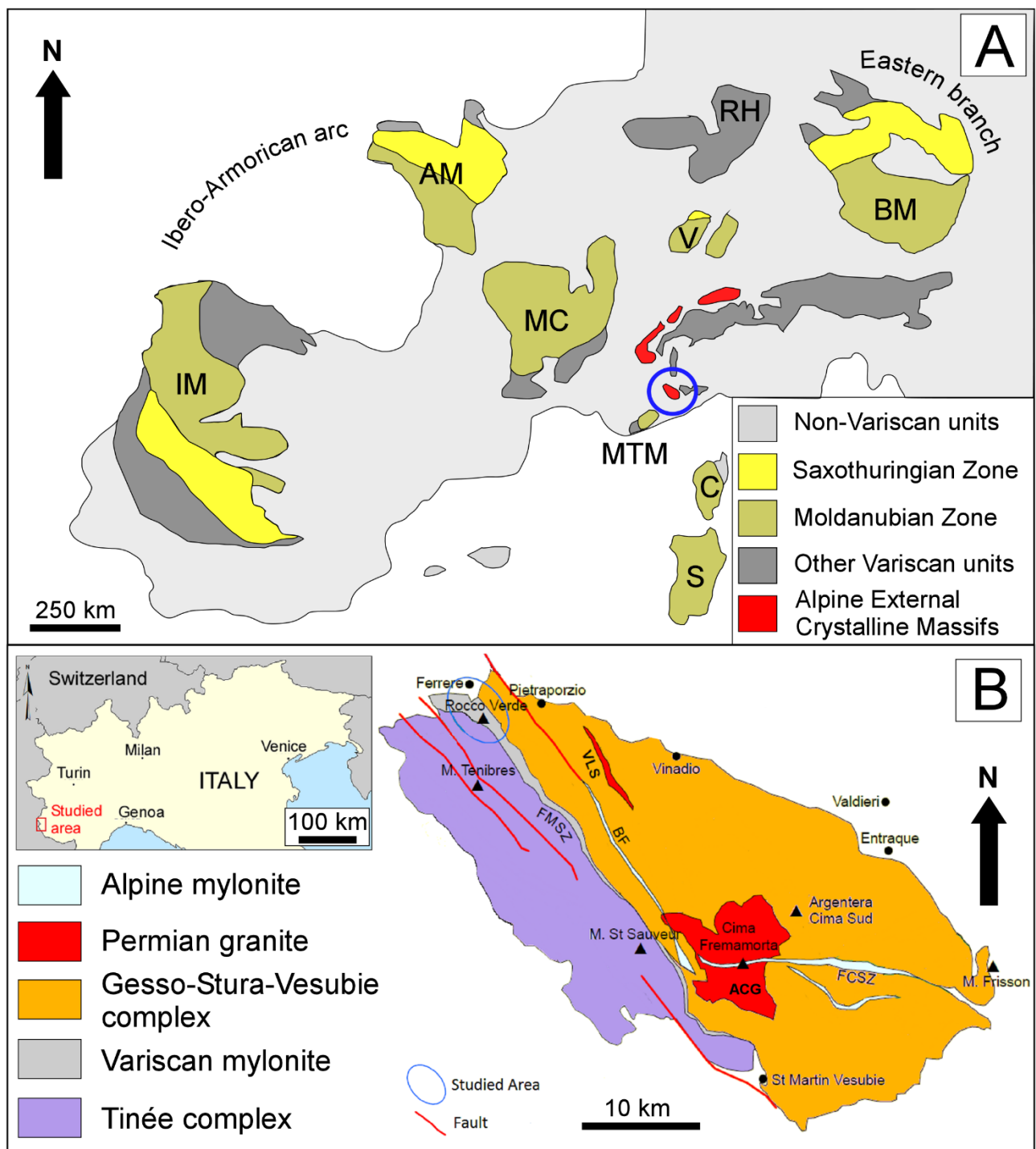


Fig.1

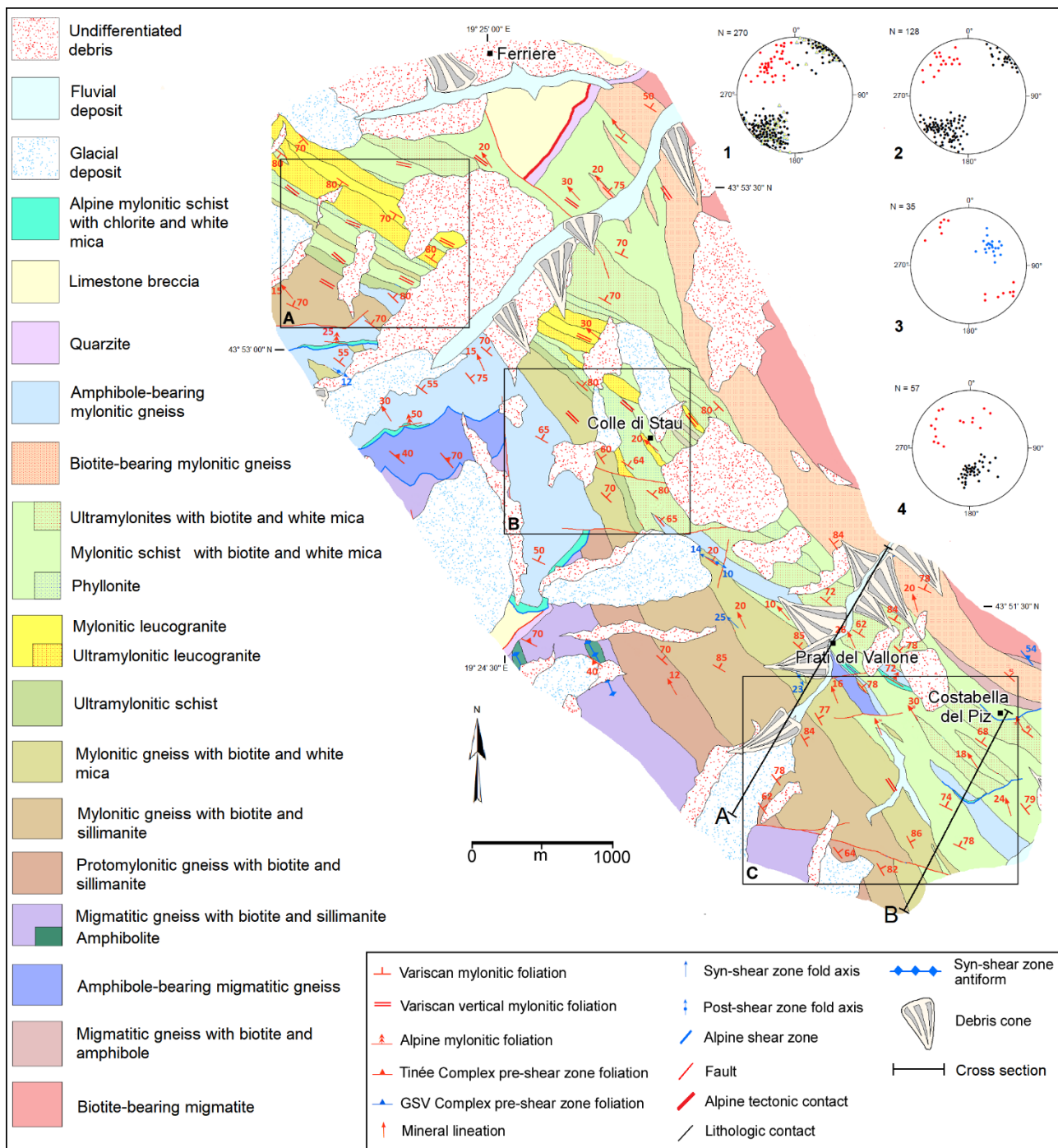
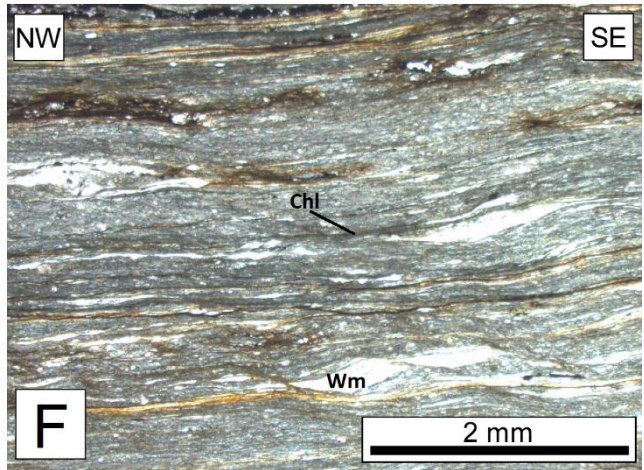
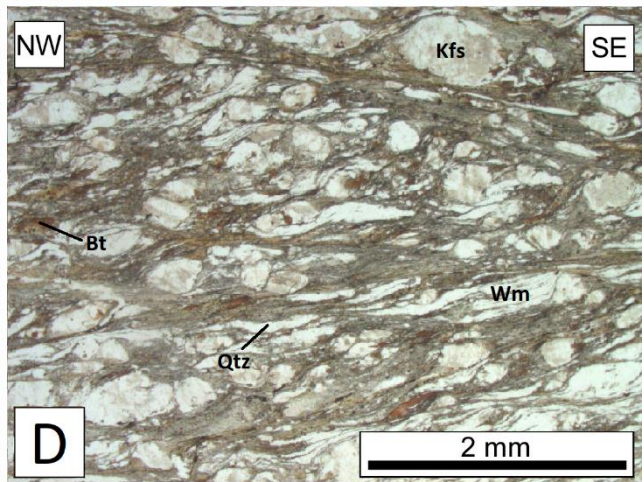
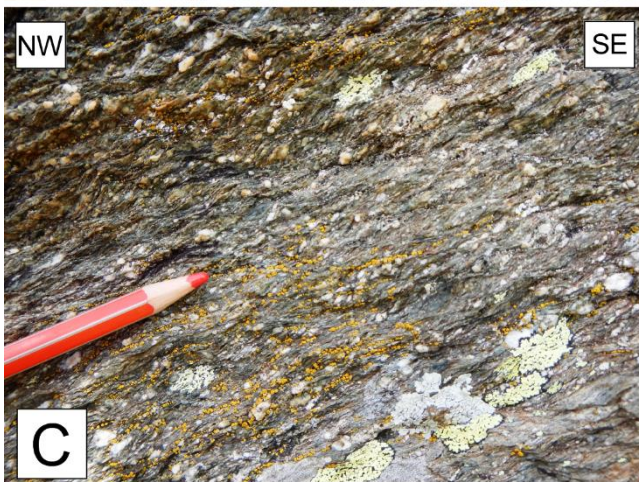
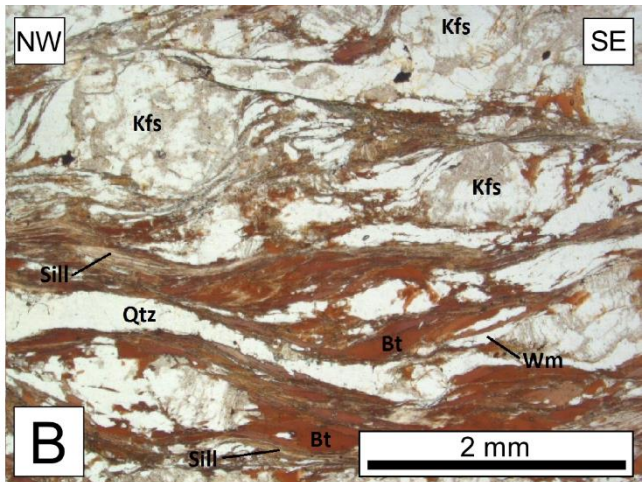


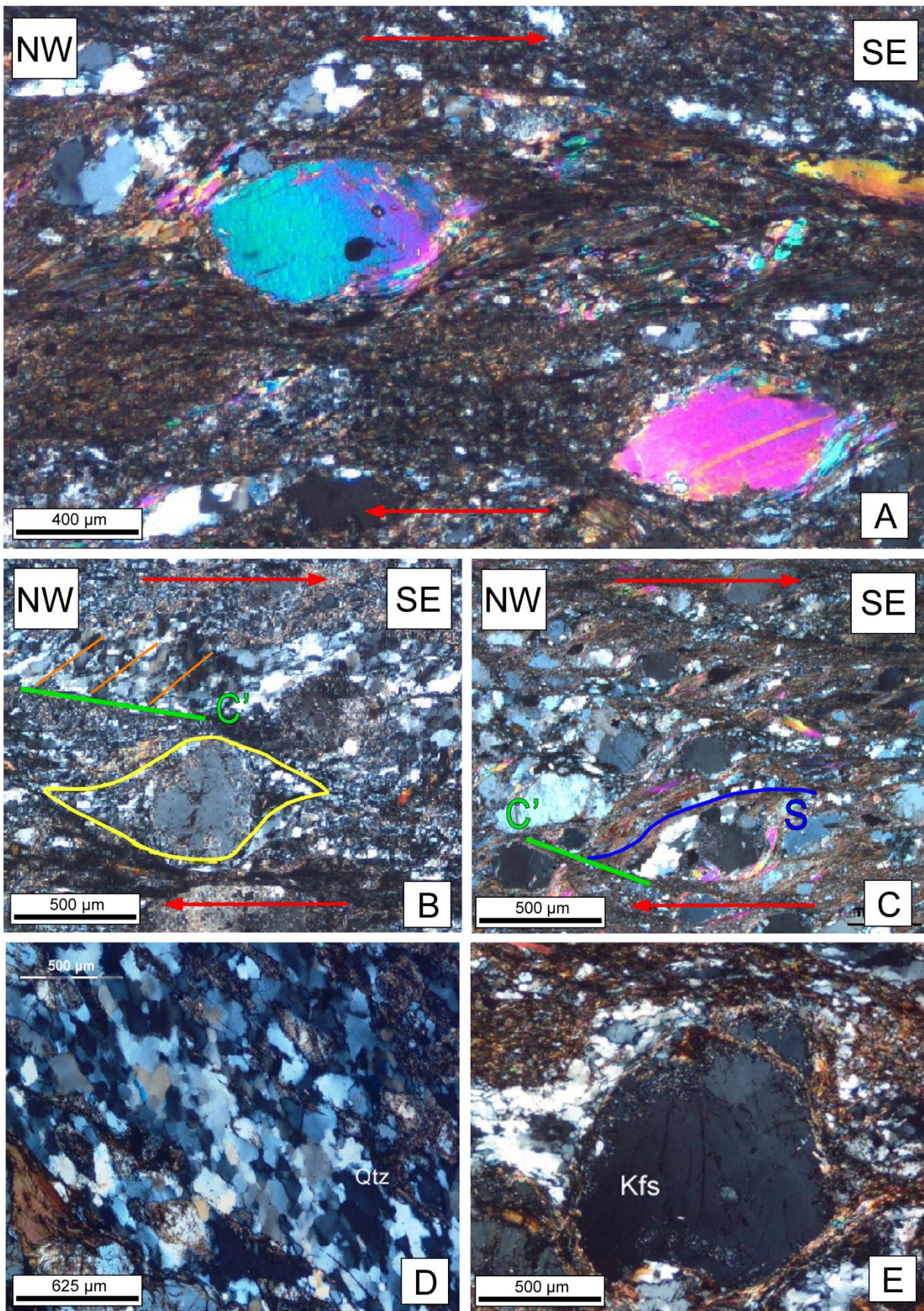
Fig.2





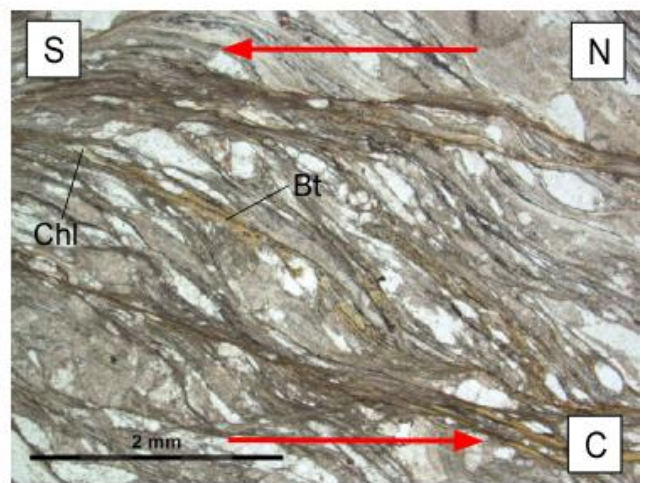
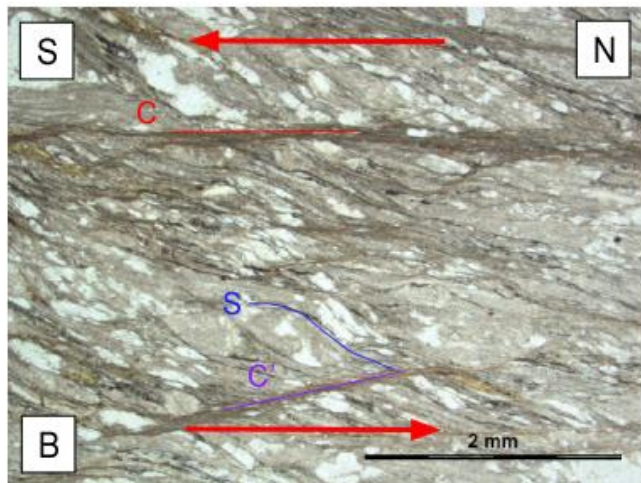
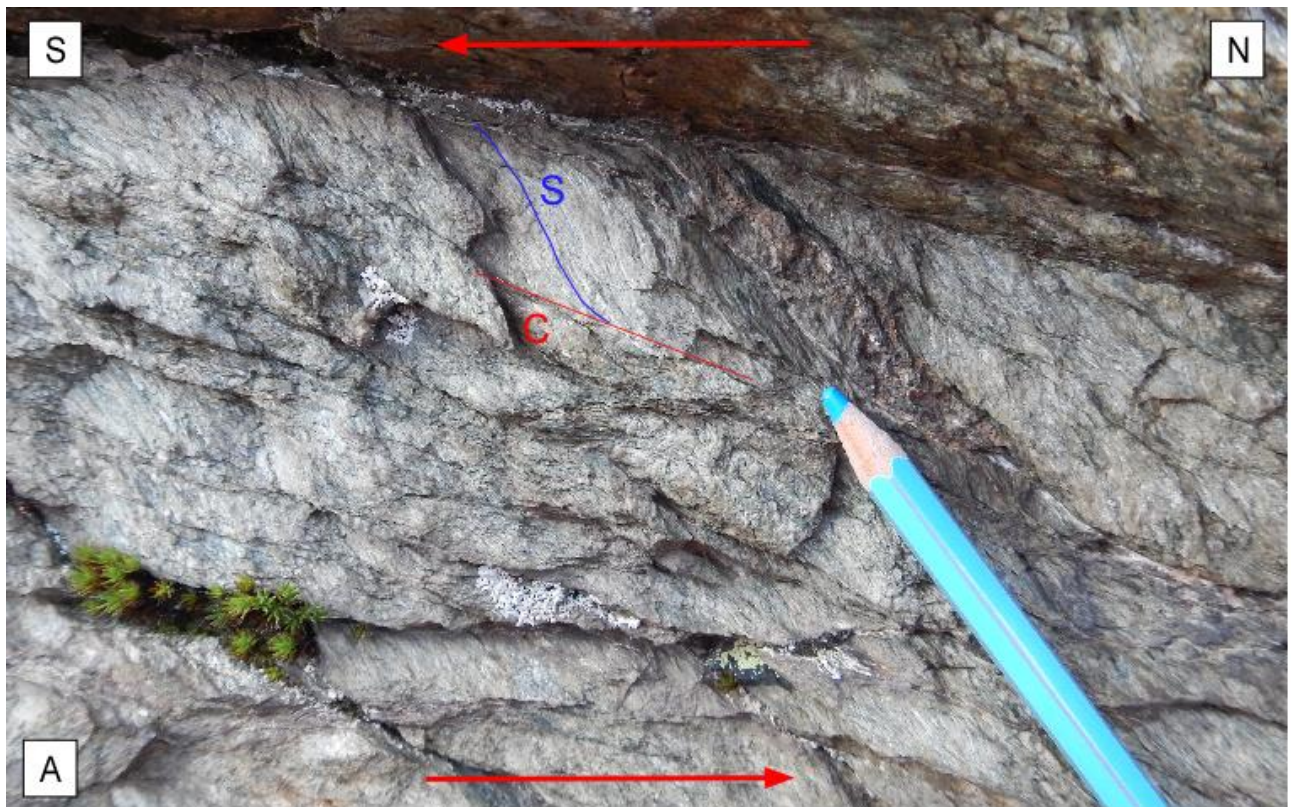
915  
916  
917  
918  
919  
920  
921  
922





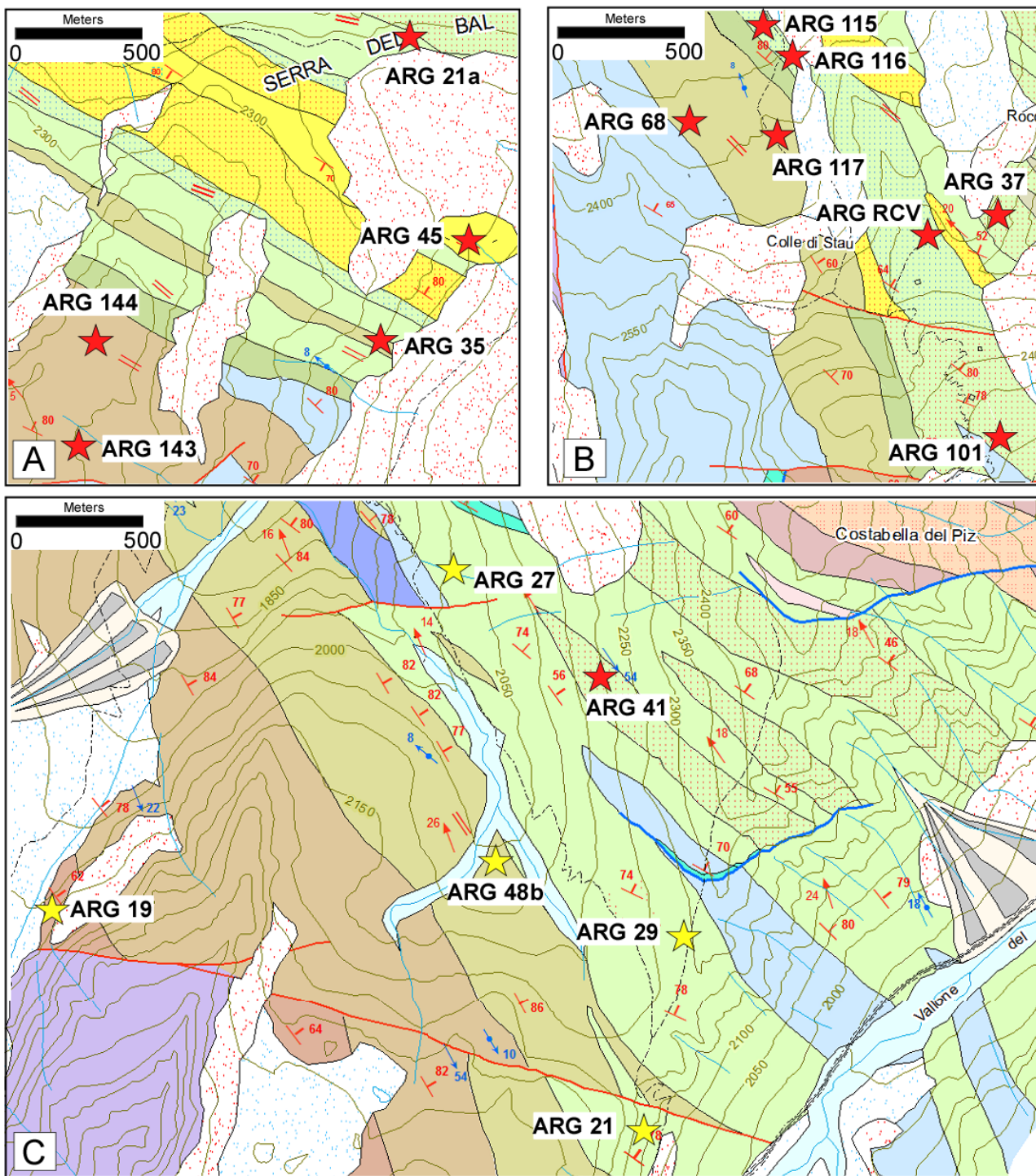
923  
924 Fig.4





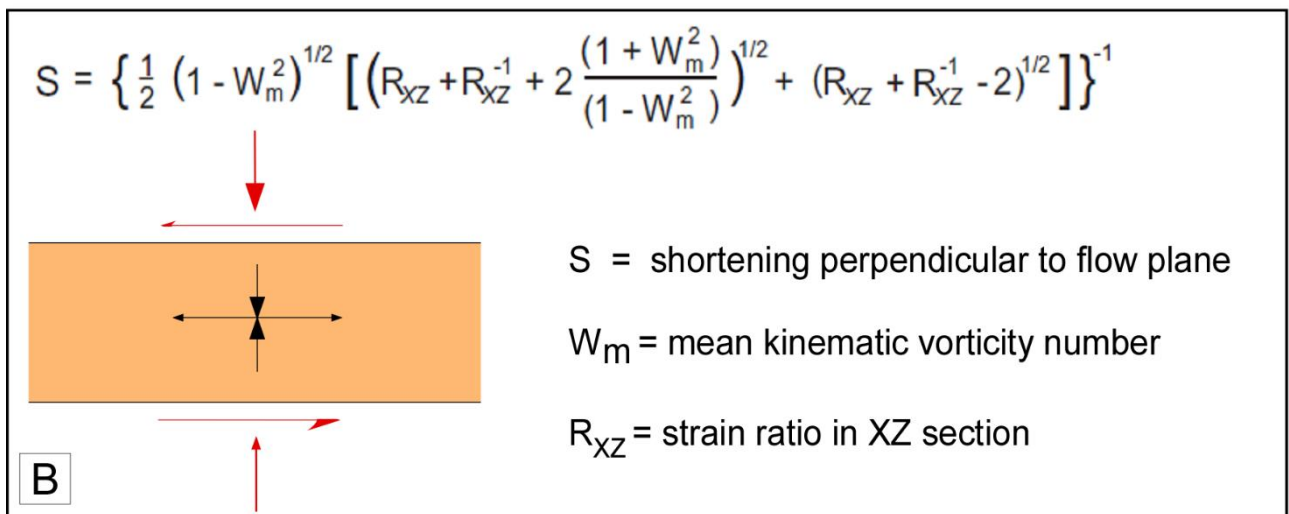
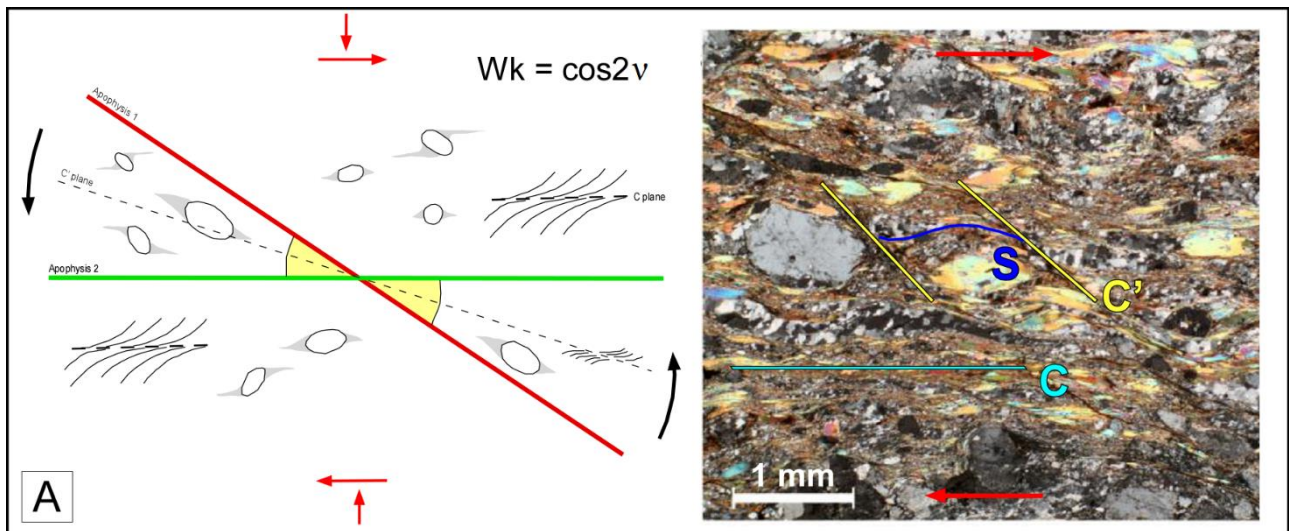
925  
926 Fig.5





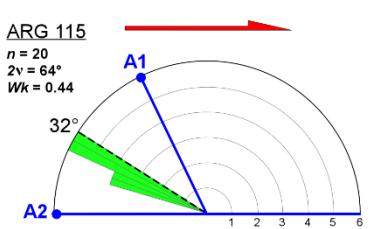
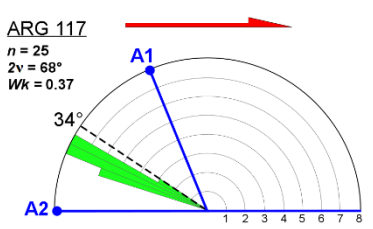
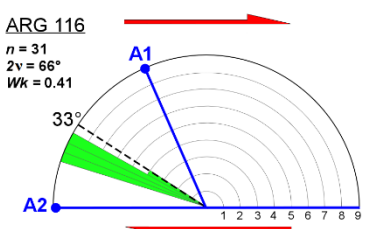
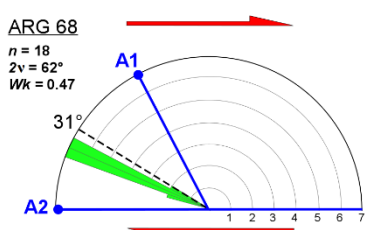
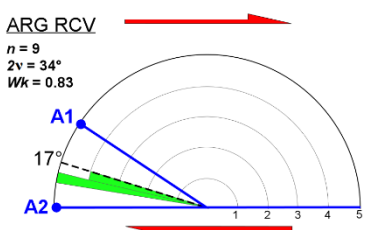
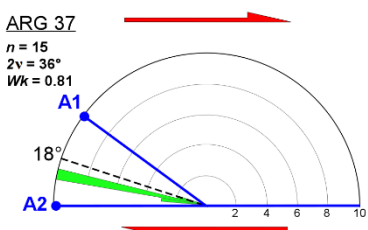
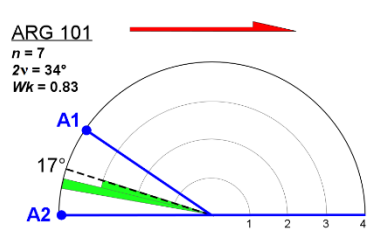
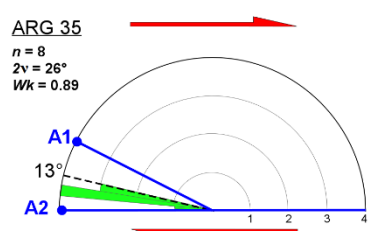
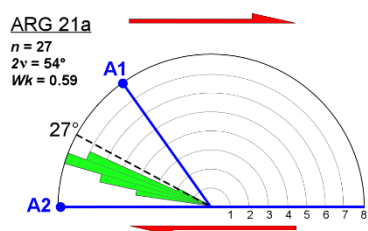
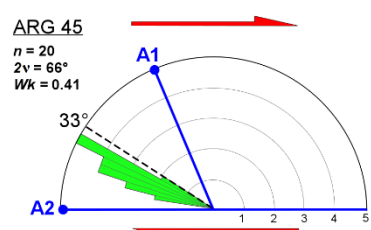
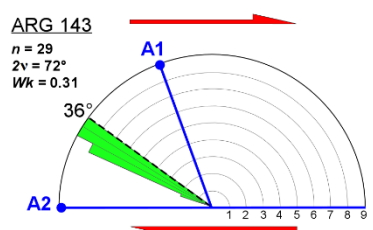
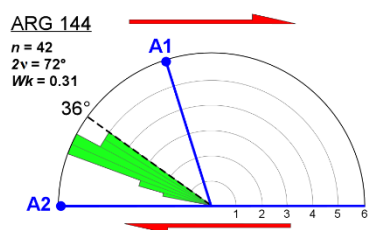
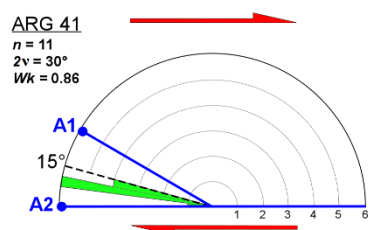
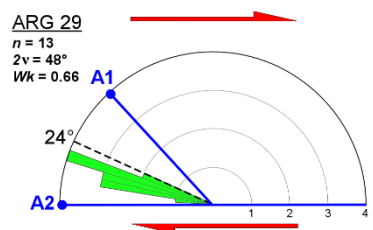
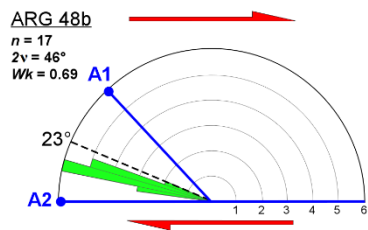
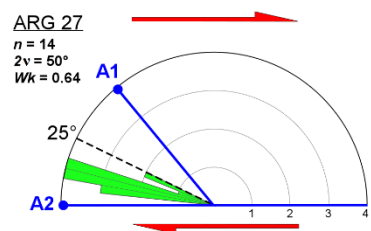
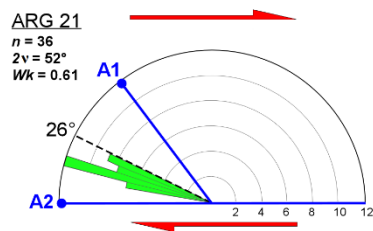
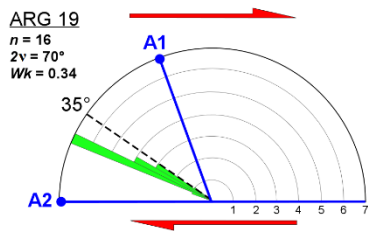
927

928 Fig.6



929

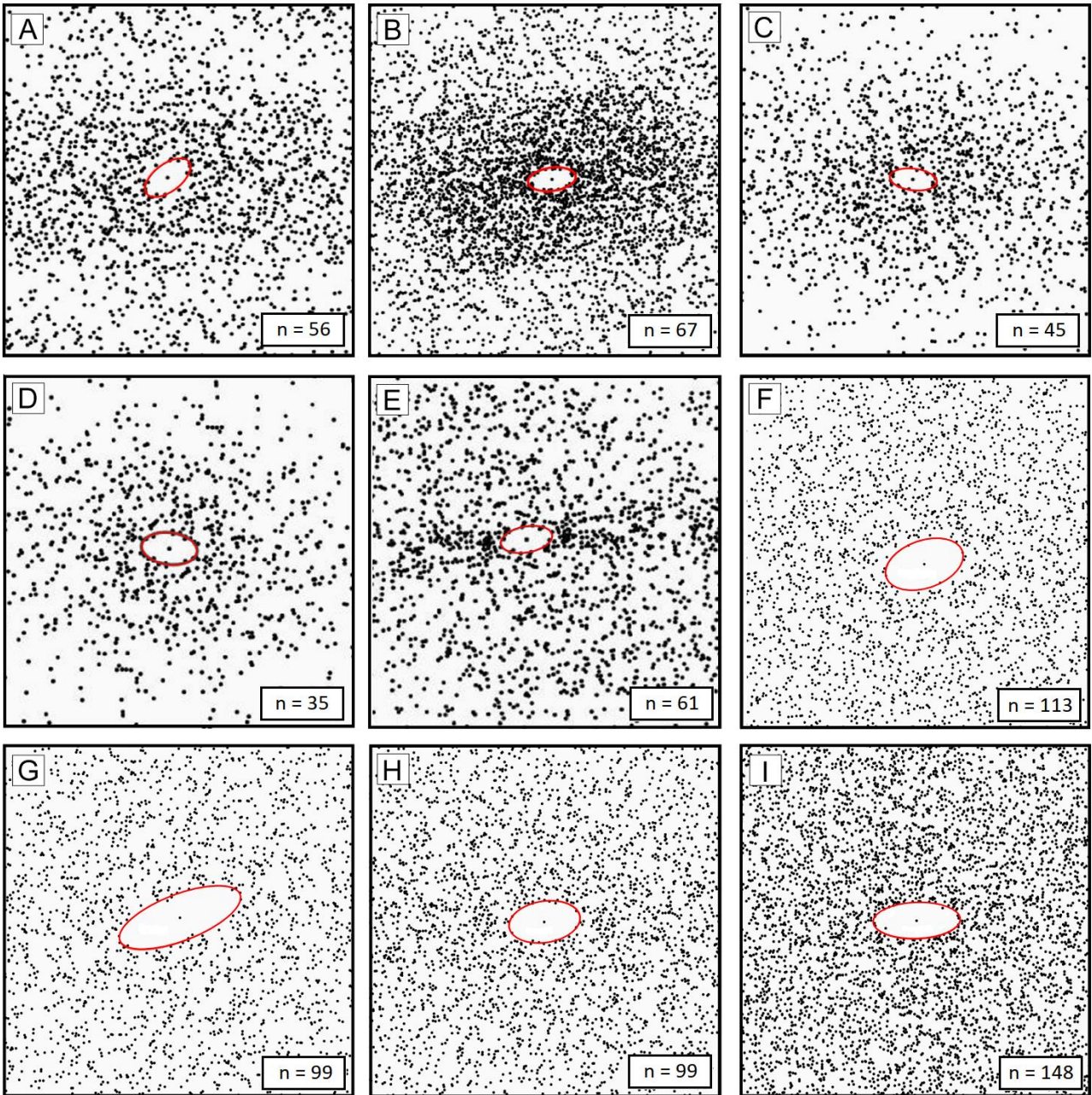
930 Fig.7



931  
932

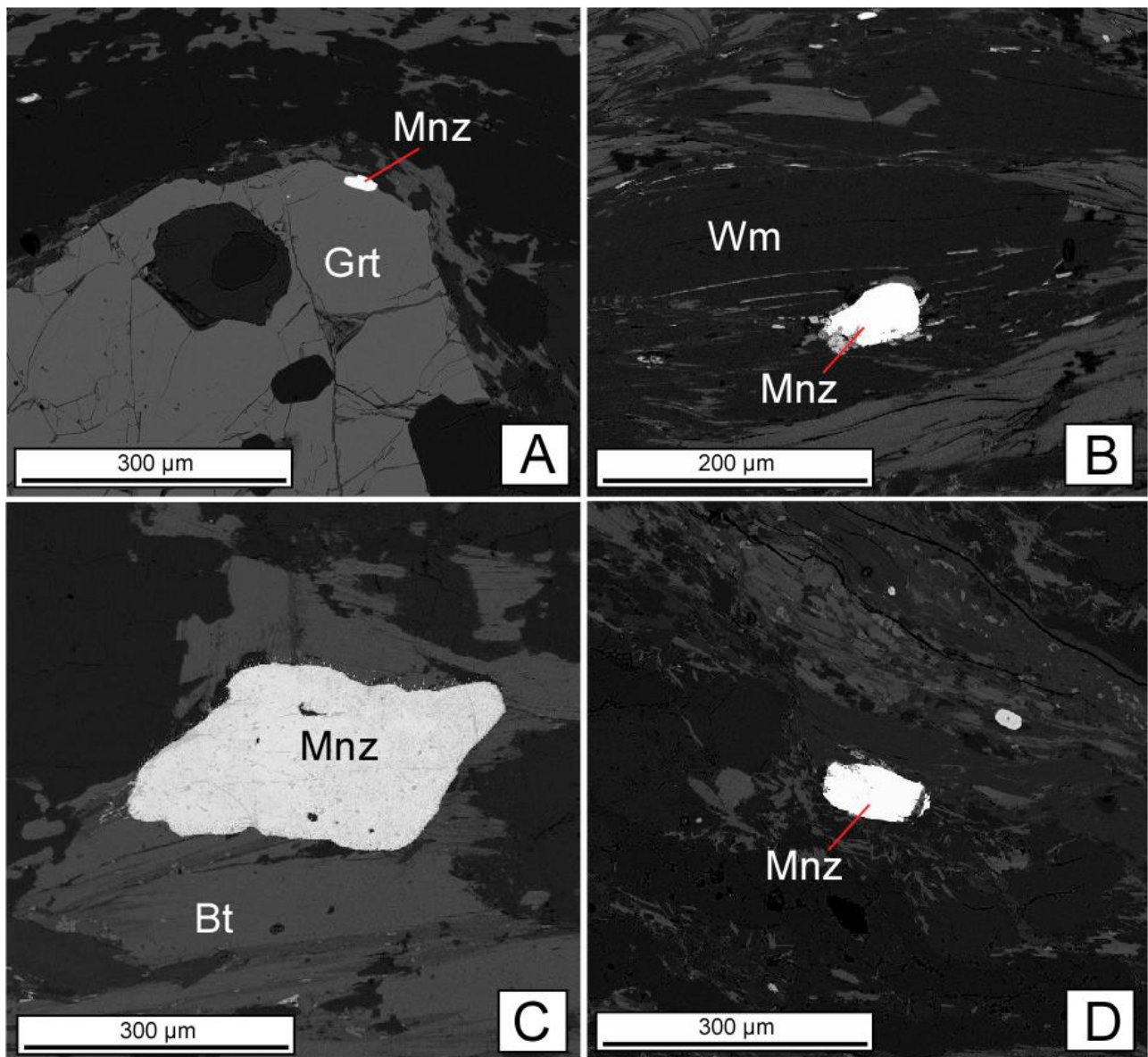
Fig.8





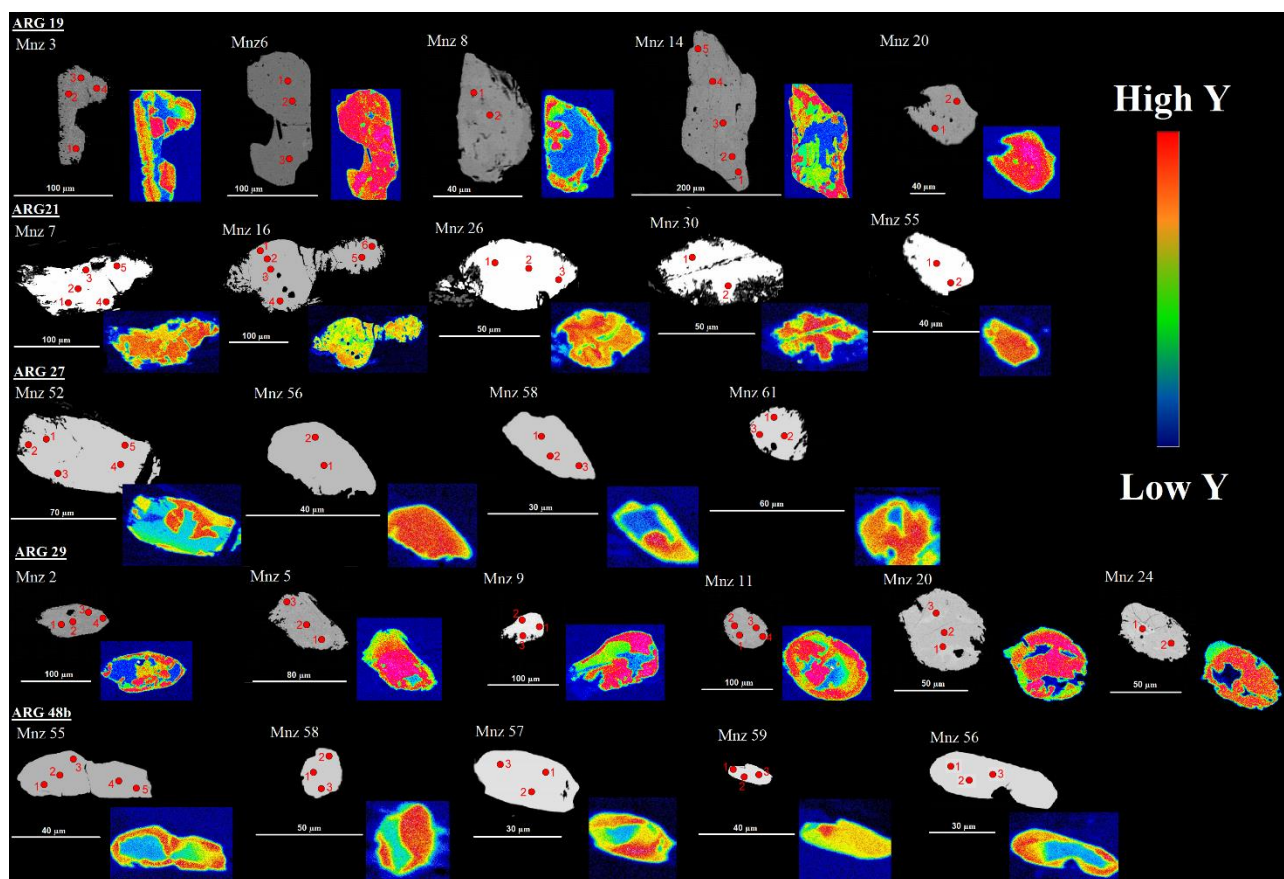
933

934 Fig.9



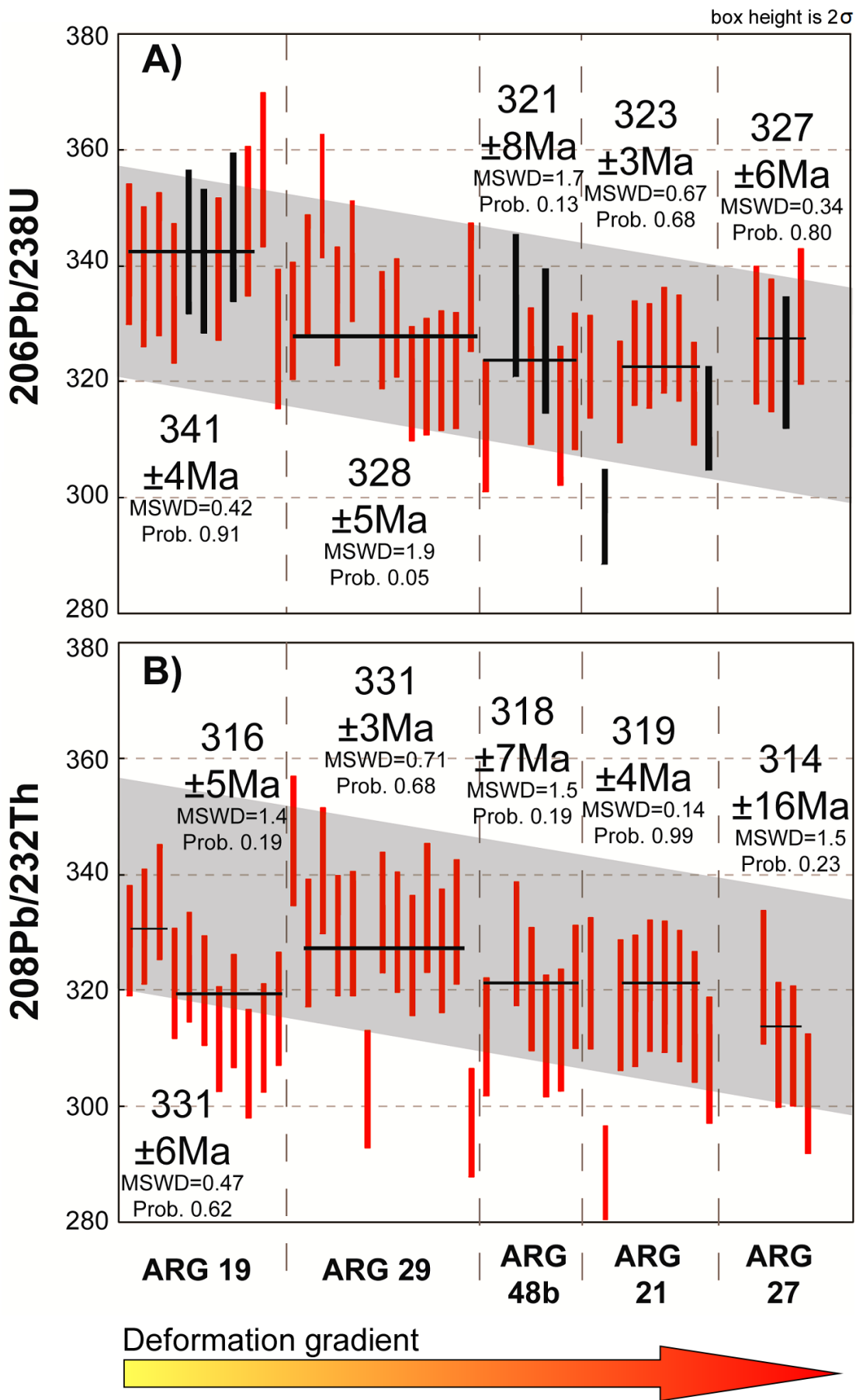
935  
936 Fig.10





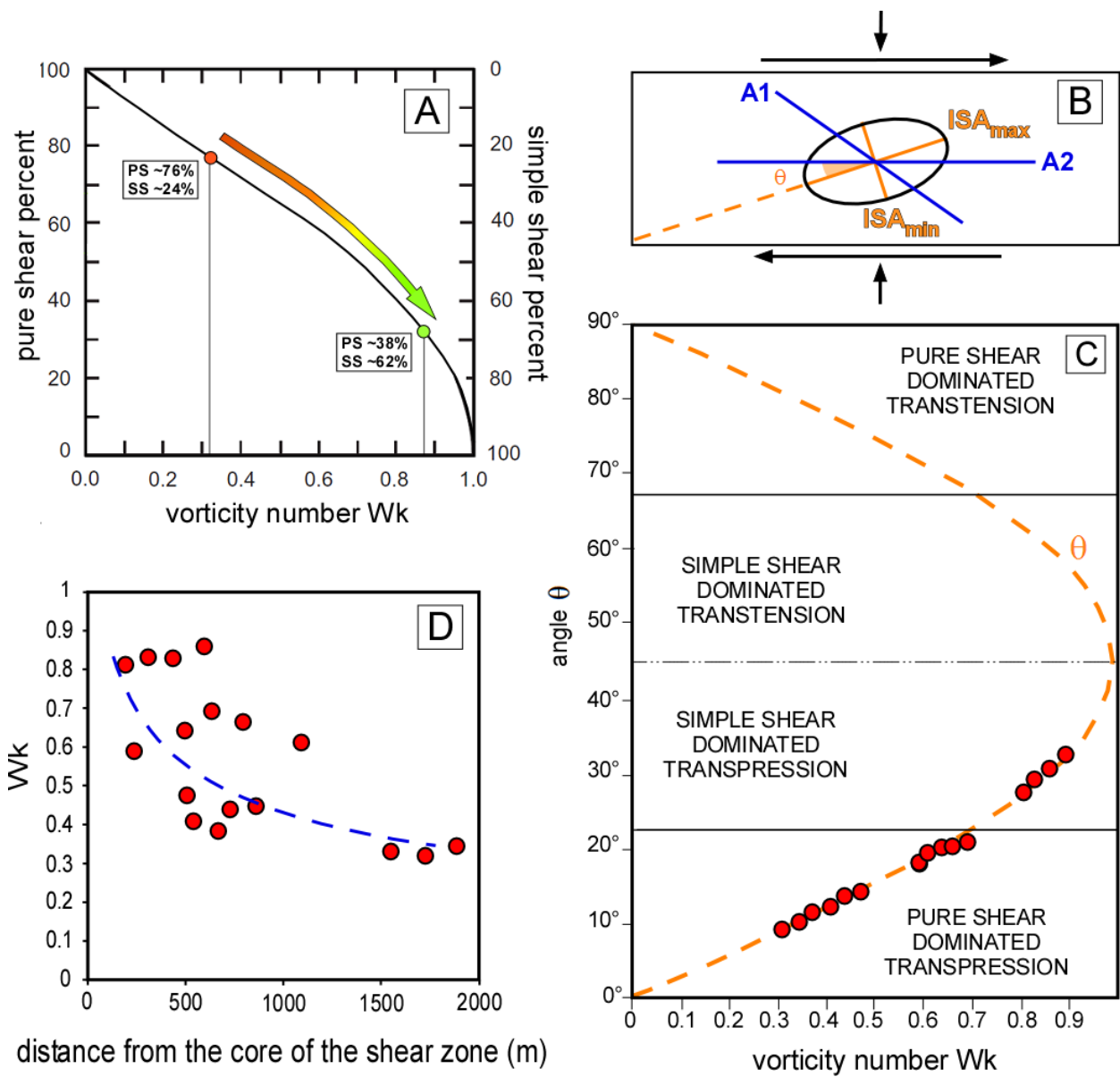
937

938 Fig.11



939

940 Fig.12

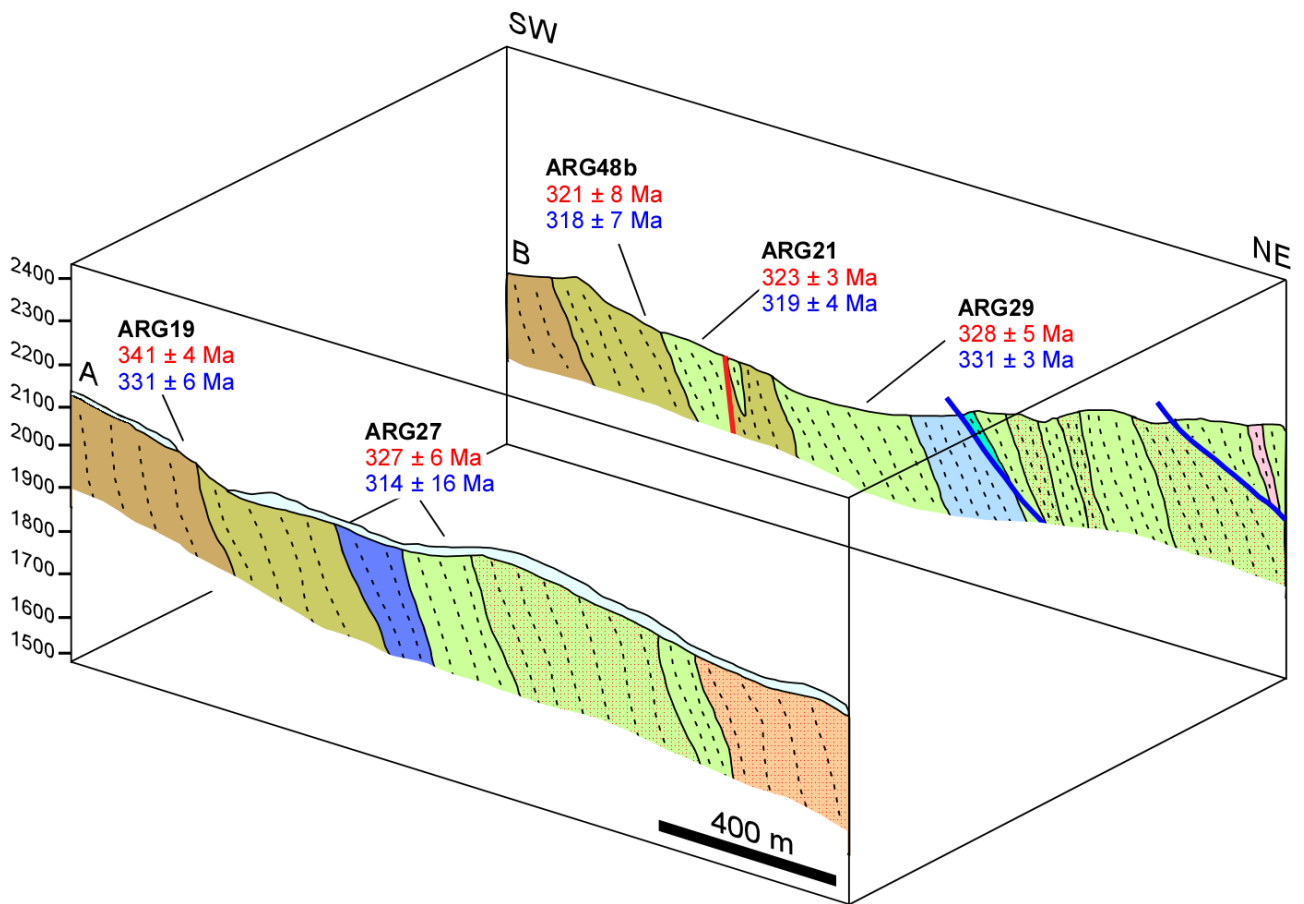


941

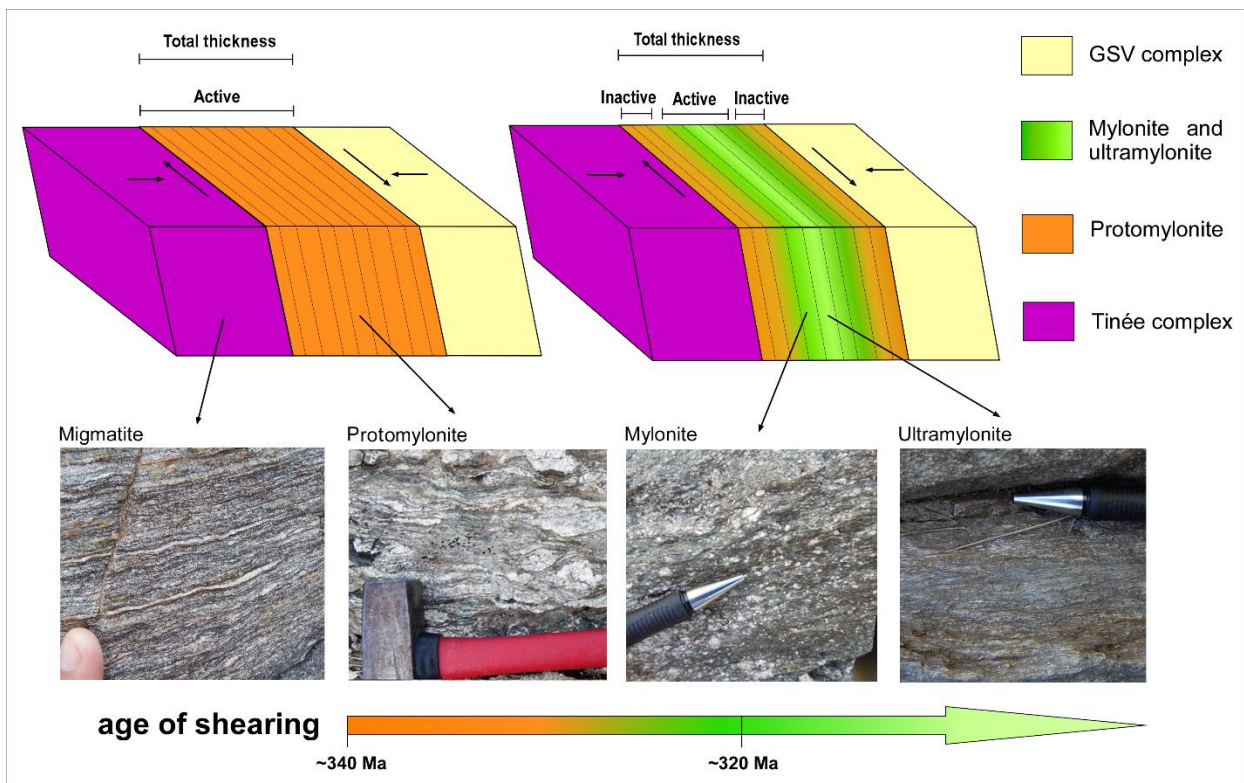
942

Fig.13





943  
944 Fig.14



945  
946 Fig.15

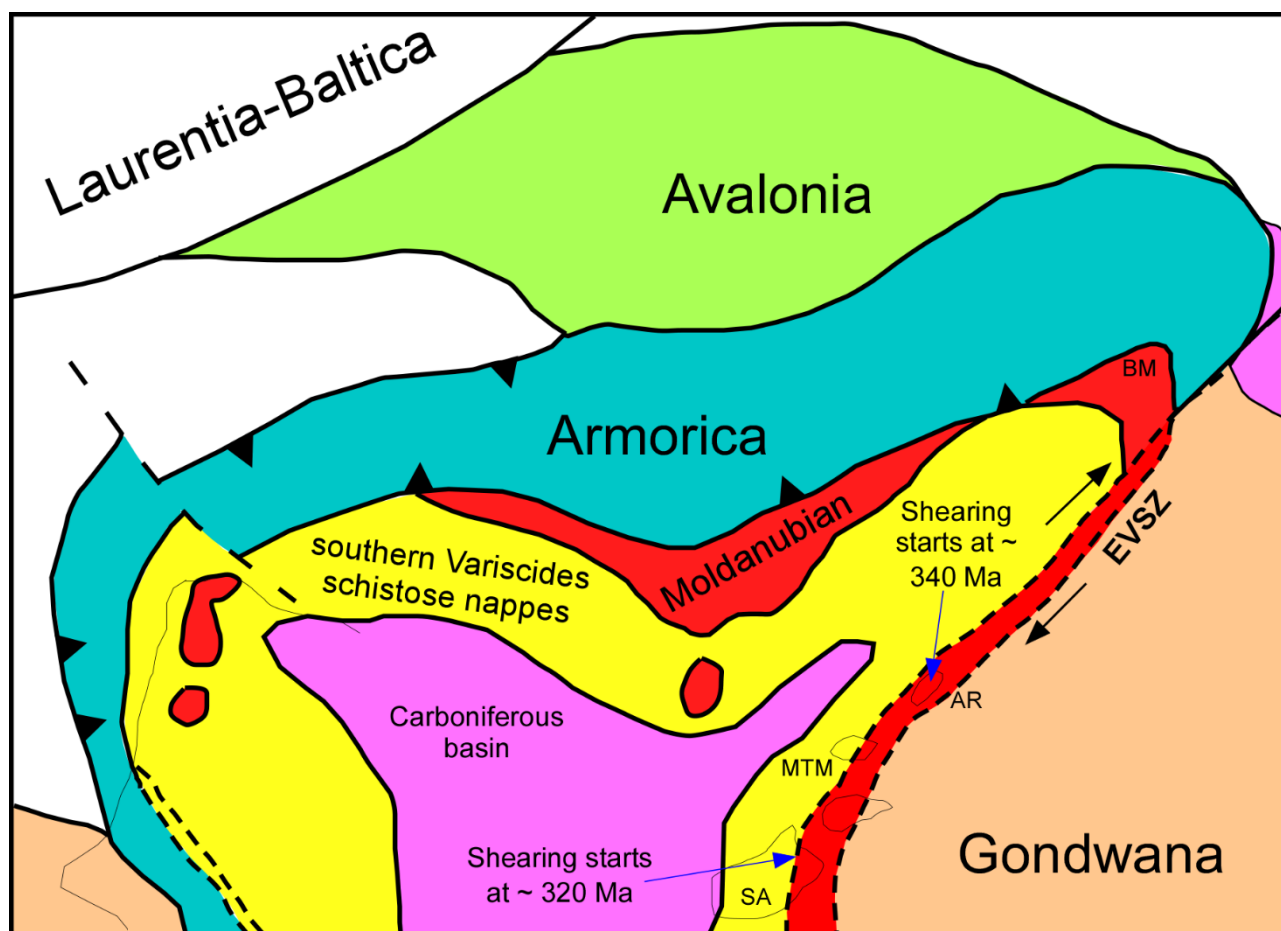


Fig.16

SAMPLE	N	v max	2v	Wk	Angle θ	n	Rxz	Shortening (S)	Stretching (1/S)	Deformation	Transect
ARG 144	42	36°	72°	0,31	9°	67	1,88	0,74	1,35	Protomylonite	A
ARG 143	29	36°	72°	0,31	9°	56	1,99	0,72	1,38	Protomylonite	A
ARG45	20	33°	66°	0,41	12°	-	-	-	-	Mylonite	A
ARG 21a	27	27°	54°	0,59	18°	45	2,1	0,74	1,35	Mylonite	A
ARG 35	8	13°	26°	0,89	31°	-	-	-	-	Ultramylonite	A
ARG 101	7	17°	34°	0,83	28°	-	-	-	-	Ultramylonite	B
ARG 37	15	18°	36°	0,81	27°	-	-	-	-	Ultramylonite	B
ARG RCV	9	17°	34°	0,83	28°	-	-	-	-	Ultramylonite	B
ARG 68	18	31°	62°	0,47	14°	35	1,87	0,76	1,31	Mylonite	B
ARG 116	31	33°	66°	0,41	12°	-	-	-	-	Mylonite	B
ARG 117	25	34°	68°	0,37	11°	61	2,05	0,71	1,39	Mylonite	B
ARG 115	20	32°	64°	0,44	13°	-	-	-	-	Mylonite	B
ARG 19	16	35°	70°	0,34	10°	113	1,71	0,78	1,28	Protomylonite	C
ARG 21	36	26°	52°	0,61	19°	99	2,85	0,63	1,59	Mylonite	C
ARG 27	14	25°	50°	0,64	20°	99	1,75	0,81	1,23	Mylonite	C
ARG 48B	17	23°	46°	0,69	21°	-	-	-	-	Mylonite	C
ARG 29	13	24°	48°	0,66	20°	148	2,46	0,72	1,38	Mylonite	C
ARG 41	11	15°	30°	0,86	30°	-	-	-	-	Ultramylonite	C

Tab.1

956

957

958

Identifier	Comments	<sup>207</sup> Pb/ <sup>206</sup> Pb			<sup>207</sup> Pb/ <sup>235</sup> U			<sup>206</sup> Pb/ <sup>238</sup> U			<sup>208</sup> Pb/ <sup>232</sup> Th			Ages							
		Ratio	1s %	1s % (Prop)	Ratio	1s %	1s % (Prop)	Ratio	1s %	1s % (Prop)	Ratio	1s %	1s % (Prop)	<sup>207</sup> Pb/ <sup>206</sup> Pb	1s abs	<sup>207</sup> Pb/ <sup>235</sup> U	1s abs	<sup>206</sup> Pb/ <sup>238</sup> U	1s abs	<sup>208</sup> Pb/ <sup>232</sup> Th	1s abs
Ju08a001	begin	0,05630	0,06%	0,10%	0,64227	0,77%	1,14%	0,08274	0,10%	0,11%	0,02538	0,04%	0,04%	464	8	504	9	512	7	507	9
Ju08a003	begin	0,05708	0,06%	0,10%	0,65076	0,80%	1,18%	0,08270	0,11%	0,11%	0,02535	0,04%	0,04%	495	9	509	9	512	7	506	9
Ju08a004	begin	0,05629	0,06%	0,10%	0,63652	0,78%	1,15%	0,08203	0,10%	0,11%	0,02501	0,04%	0,04%	464	8	500	9	508	7	499	9
Ju08a015	end	0,05790	0,06%	0,10%	0,65608	0,86%	1,22%	0,08220	0,11%	0,12%	0,02522	0,04%	0,04%	526	9	512	10	509	7	503	9
Ju08a016	end	0,05609	0,06%	0,10%	0,64304	0,85%	1,20%	0,08316	0,11%	0,12%	0,02493	0,04%	0,04%	456	8	504	9	515	7	498	9
Ju08a017	end	0,05580	0,06%	0,10%	0,63342	0,84%	1,19%	0,08234	0,11%	0,12%	0,02561	0,04%	0,04%	444	8	498	9	510	7	511	9
Ju08b001	begin	0,05758	0,06%	0,14%	0,65908	0,87%	1,60%	0,08304	0,11%	0,14%	0,02527	0,04%	0,04%	514	12	514	12	514	9	504	9
Ju08b002	begin	0,05519	0,06%	0,13%	0,63537	0,85%	1,54%	0,08352	0,11%	0,14%	0,02553	0,04%	0,04%	420	10	499	12	517	9	510	9
Ju08b003	begin	0,05652	0,06%	0,14%	0,63603	0,85%	1,54%	0,08165	0,11%	0,14%	0,02510	0,04%	0,04%	473	11	500	12	506	9	501	8
Ju08b004	begin	0,05674	0,07%	0,14%	0,64005	0,86%	1,56%	0,08185	0,11%	0,14%	0,02507	0,04%	0,04%	481	12	502	12	507	9	500	8
Ju08b013	end	0,05737	0,07%	0,14%	0,64299	0,91%	1,59%	0,08135	0,11%	0,14%	0,02499	0,03%	0,04%	506	12	504	12	504	9	499	8
Ju08b014	end	0,05797	0,07%	0,14%	0,66486	0,95%	1,65%	0,08325	0,11%	0,15%	0,02562	0,04%	0,04%	529	13	518	13	515	9	511	9
Ju08b015	end	0,05482	0,07%	0,13%	0,62971	0,91%	1,57%	0,08337	0,11%	0,15%	0,02516	0,03%	0,04%	405	10	496	12	516	9	502	8
Ju08c002	begin	0,05705	0,06%	0,11%	0,64522	0,85%	1,45%	0,08209	0,11%	0,15%	0,02516	0,03%	0,04%	493	9	506	11	509	9	502	8
Ju08c003	begin	0,05590	0,06%	0,10%	0,63972	0,84%	1,43%	0,08303	0,11%	0,15%	0,02523	0,03%	0,04%	448	8	502	11	514	9	504	8
Ju08c004	begin	0,05766	0,07%	0,11%	0,65281	0,89%	1,48%	0,08217	0,11%	0,15%	0,02544	0,04%	0,04%	517	10	510	12	509	9	508	8
Ju08c013	end	0,05615	0,07%	0,11%	0,62536	0,88%	1,43%	0,08075	0,11%	0,15%	0,02484	0,03%	0,04%	458	9	493	11	501	9	496	8
Ju08c014	end	0,05742	0,07%	0,11%	0,65902	0,95%	1,53%	0,08325	0,11%	0,15%	0,02537	0,03%	0,04%	508	10	514	12	515	9	506	8
Ju08c015	end	0,05570	0,07%	0,11%	0,64087	0,93%	1,49%	0,08345	0,11%	0,15%	0,02541	0,04%	0,04%	440	9	503	12	517	9	507	8
No23a001	begin	0,05641	0,06%	0,07%	0,64883	0,85%	1,22%	0,08347	0,11%	0,14%	0,02531	0,00032	0,00037	469	6	508	10	517	9	505	7
No23a001	begin	0,05675	0,06%	0,07%	0,63471	0,85%	1,21%	0,08113	0,11%	0,14%	0,02501	0,00032	0,00037	482	6	499	10	503	9	499	7
No23a001	begin	0,05671	0,06%	0,07%	0,65188	0,87%	1,24%	0,08336	0,12%	0,15%	0,02557	0,00032	0,00037	480	6	510	10	516	9	510	7
No23a001	begin	0,0563	0,06%	0,07%	0,63964	0,86%	1,22%	0,08241	0,12%	0,15%	0,02515	0,00032	0,00037	464	6	502	10	510	9	502	7
No23a002	end	0,05692	0,06%	0,07%	0,65378	0,93%	1,29%	0,0833	0,12%	0,15%	0,02544	0,00032	0,00037	488	6	511	10	516	9	508	7
No23a002	end	0,057	0,06%	0,07%	0,65193	0,91%	1,27%	0,08295	0,12%	0,15%	0,02515	0,00032	0,00037	492	6	510	10	514	9	502	7
No23a002	end	0,05599	0,06%	0,07%	0,6331	0,89%	1,24%	0,082	0,12%	0,15%	0,02532	0,00032	0,00037	452	6	498	10	508	9	505	7
No23b001	begin	0,05627	0,06%	0,07%	0,63949	0,93%	1,03%	0,08245	0,12%	0,12%	0,02519	0,00032	0,00039	463	6	502	8	511	8	503	8
No23b001	begin	0,05716	0,06%	0,07%	0,64833	0,91%	1,02%	0,08229	0,12%	0,12%	0,0256	0,00033	0,0004	498	6	507	8	510	8	511	8
No23b001	begin	0,05618	0,06%	0,07%	0,64229	0,91%	1,02%	0,08294	0,12%	0,12%	0,02499	0,00032	0,00039	459	6	504	8	514	8	499	8
No23b001	begin	0,05676	0,06%	0,07%	0,64873	0,89%	1,01%	0,08291	0,12%	0,12%	0,02554	0,00032	0,00039	482	6	508	8	513	8	510	8
No23b002	end	0,05627	0,07%	0,08%	0,63878	0,95%	1,06%	0,08233	0,12%	0,13%	0,02532	0,00031	0,00038	463	6	502	8	510	8	505	8
No23b002	end	0,05664	0,06%	0,07%	0,64804	0,93%	1,04%	0,08297	0,12%	0,13%	0,02527	0,00031	0,00038	478	6	507	8	514	8	504	8

Tab.2

Sample	Identifier	Mnz#	spot locatio	Zoning	Data for Wetherill plot <sup>3</sup>						Rho	Ages <sup>3</sup>						U-Pb disc <sup>4</sup>		Pb Concordant age <sup>4</sup>						
					<sup>207</sup> Pb/ <sup>235</sup> Pb	1s abs	<sup>207</sup> Pb/ <sup>235</sup> U	1s abs	1s abs	1s abs		<sup>206</sup> Pb/ <sup>238</sup> Th	1s abs	<sup>206</sup> Pb/ <sup>238</sup> Pb	1s abs	<sup>207</sup> Pb/ <sup>235</sup> U	1s abs	<sup>206</sup> Pb/ <sup>238</sup> Th	1s abs	U-Pb disc	U-Th disc <sup>4</sup>	2s abs				
ARG 19	No23a001	Mnz14	core	low-Y	0.05060	0.00060	0.37949	0.00711	0.05446	0.00096	0.9	0.01639	0.00024	223	3	327	6	342	6	329	5	-4.6	3.9			
	No23a001	Mnz14	core	int-Y	0.04850	0.00058	0.35984	0.00677	0.05384	0.00095	0.9	0.01651	0.00024	124	1	312	6	338	6	331	5	-8.3	2.1			
	No23a001	Mnz14	rim	high-Y	0.04718	0.00054	0.35209	0.00655	0.05419	0.00097	1.0	0.01672	0.00025	58	1	306	6	340	6	335	5	-11.1	1.5			
	No23a001	Mnz14	rim	high-Y	0.04719	0.00054	0.34671	0.00644	0.05337	0.00095	1.0	0.01602	0.00023	59	1	302	6	335	6	321	5	-10.9	4.2			
	No23a001	Mnz14	rim	high-Y	0.05304	0.00063	0.39997	0.00750	0.05482	0.00098	0.9	0.01616	0.00023	331	4	342	6	344	6	324	5	-0.7	5.8	341	11	
	No23a001	Mnz14	core	low-Y	0.05362	0.00060	0.40053	0.00737	0.05427	0.00097	1.0	0.01596	0.00023	355	4	342	6	341	6	320	5	0.4	6.1	344	10	
	No23a001	Mnz6	core	high-Y	0.04672	0.00052	0.34731	0.00641	0.05405	0.00097	1.0	0.01554	0.00022	35	0	303	6	339	6	312	4	-12.1	8.2			
	No23a001	Mnz3	core	low-Y	0.05366	0.00075	0.40986	0.00859	0.05523	0.0101	0.9	0.01578	0.00024	357	5	349	7	347	6	316	5	0.6	8.7	348	12	
	No23a001	Mnz3	core	low-Y	0.05091	0.00074	0.38909	0.00823	0.05540	0.0102	0.9	0.01533	0.00023	237	3	334	7	348	6	308	5	-4.2	11.5			
	No23a001	Mnz8	core	low-Y	0.05012	0.00073	0.39204	0.00837	0.05684	0.0105	0.9	0.01555	0.00023	201	3	336	7	356	7	312	5	-6.1	12.5			
	No23a001	Mnz8	rim	high-Y	0.06046	0.00089	0.43421	0.00917	0.05209	0.00095	0.9	0.01580	0.00024	620	9	366	8	327	6	317	5	10.6	3.2			
ARG 29	No23b001	Mnz5	core	high-Y	0.04671	0.00064	0.33727	0.00559	0.05260	0.00080	0.9	0.01725	0.00028	34	0	295	5	330	5	346	6	-12.0	-4.6			
	No23b001	Mnz5	rim/core	low-Y	0.04793	0.00067	0.35617	0.00602	0.05387	0.00083	0.9	0.01637	0.00027	96	1	309	5	338	5	328	5	-9.3	3.0			
	No23b001	Mnz2	core	low-Y	0.04709	0.00054	0.36473	0.00547	0.05610	0.00085	1.0	0.01699	0.00027	54	1	316	5	362	5	341	5	-11.4	3.2			
	No23b001	Mnz2	core	high/int-Y	0.04631	0.00056	0.33850	0.00520	0.05301	0.00081	1.0	0.01643	0.00026	14	0	296	5	333	5	329	5	-12.5	1.1			
	No23b001	Mnz9	rim	high-Y	0.04648	0.00061	0.34793	0.00565	0.05427	0.00083	0.9	0.01645	0.00026	23	0	303	5	341	5	330	5	-12.4	3.2			
	No23b001	Mnz9	core	low-Y	0.18607	0.00259	1.52869	0.02448	0.05974	0.00093	1.0	0.01511	0.00025	2708	38	942	15	374	6	303	5	60.3	19.0			
	No23b001	Mnz11	core	low-Y	0.04845	0.00058	0.34997	0.00538	0.05234	0.00080	1.0	0.01663	0.00026	121	1	305	5	329	5	333	5	-7.9	-1.4			
	No23b001	Mnz11	core	low-Y	0.04926	0.00058	0.35799	0.00544	0.05268	0.00081	1.0	0.01646	0.00026	160	2	311	5	331	5	330	5	-6.5	0.3			
	No23b001	Mnz11	rim	high-Y	0.05338	0.00064	0.37450	0.00578	0.05085	0.00078	1.0	0.01626	0.00026	345	4	323	5	320	5	326	5	-1.0	-2.0			
	No23b001	Mnz20	core	high-Y	0.04698	0.00072	0.33071	0.00590	0.05104	0.00080	0.9	0.01667	0.00027	48	1	290	5	321	5	334	5	-10.6	-4.1			
	No23b001	Mnz20	rim	low-Y	0.04901	0.00074	0.34441	0.00616	0.05121	0.00082	0.9	0.01630	0.00026	148	2	301	5	322	5	327	5	-7.1	-1.5			
	No23b001	Mnz24	core	high-Y	0.04687	0.00070	0.33064	0.00584	0.05121	0.00079	0.9	0.01655	0.00026	43	1	290	5	322	5	332	5	-11.0	-3.1			
	No23b001	Mnz24	core	low-Y	0.05828	0.00114	0.43250	0.00934	0.05354	0.00088	0.8	0.01482	0.00023	540	11	365	8	336	5	297	5	7.9	11.6			
	ARG 48b	Ju08c006	Mnz58	Core	igh-Y/low	0.05115	0.00092	0.35022	0.00773	0.04967	0.00130	0.8	0.01556	0.00025	248	4	305	7	312	6	312	5	-2.5	0.1		
Ju08c007		Mnz59	Core	High-Y	0.05339	0.00112	0.35447	0.01353	0.07418	0.00098	0.7	0.02130	0.00035	345	7	405	11	461	9	426	7	-4.4	7.7			
Ju08c008		Mnz57	Core	igh-Y/low	0.05361	0.00100	0.39211	0.00893	0.05303	0.00096	0.8	0.01636	0.00026	355	7	336	8	333	6	328	5	0.8	1.5	334	12	
Ju08c009		Mnz56	Core	Medium-L	0.05584	0.00106	0.39324	0.00900	0.05105	0.00093	0.8	0.01597	0.00026	446	8	337	8	321	6	320	5	4.7	0.2			
Ju08c010		Mnz56	Core	Low-Y	0.05269	0.00115	0.37788	0.00964	0.05204	0.00098	0.7	0.01557	0.00026	315	7	325	8	327	6	312	5	-0.5	4.5	327	12	
Ju08c011		Mnz55	Rim	Medium-L	0.05513	0.00129	0.37930	0.01018	0.04995	0.00094	0.7	0.01562	0.00026	417	10	327	9	314	6	313	5	3.8	0.3			
Ju08c012		Mnz55	Core	Low-Y	0.04840	0.00093	0.33991	0.00792	0.05091	0.00093	0.8	0.01599	0.00026	219	2	297	7	320	6	321	5	-7.7	-0.2			
ARG21		Ju08a006	Mnz55	Core	High-Y	0.05031	0.00085	0.35590	0.00626	0.05132	0.00070	0.8	0.01602	0.00028	209	4	309	5	323	4	321	6	-4.4	0.4		
	Ju08a007	Mnz30	Core	High-Y	0.05196	0.00087	0.33730	0.00594	0.04713	0.00064	0.8	0.01430	0.00025	284	5	295	5	297	4	287	6	-0.6	3.3	297	8	
	Ju08a008	Mnz26	Core	High-Y	0.05001	0.00083	0.34893	0.00612	0.05062	0.00069	0.8	0.01583	0.00028	195	3	304	5	318	4	317	6	-4.7	0.3			
	Ju08a009	Mnz7	Core	High-Y	0.04879	0.00081	0.34771	0.00610	0.05170	0.00071	0.8	0.01587	0.00028	138	2	303	5	325	4	318	6	-7.2	2.1			
	Ju08a010	Mnz7	Core	High-Y	0.04893	0.00082	0.34800	0.00614	0.05161	0.00071	0.8	0.01600	0.00028	144	2	303	5	324	4	321	6	-7.0	1.1			
	Ju08a011	Mnz16	Core	Medium-L	0.05155	0.00095	0.36991	0.00661	0.05295	0.00072	0.8	0.01599	0.00028	266	3	309	6	327	5	321	6	-2.4	2.0			
	Ju08a012	Mnz16	Rim	High-Y	0.04985	0.00085	0.35361	0.00638	0.05184	0.00072	0.8	0.01591	0.00028	188	3	306	6	326	5	319	6	-5.3	2.1			
	Ju08a013	Mnz16	Rim	High-Y	0.04849	0.00081	0.33799	0.00598	0.05056	0.00070	0.8	0.01573	0.00028	123	2	296	5	318	4	315	6	-7.5	0.8			
	Ju08a014	Mnz16	Core	High-Y	0.05254	0.00092	0.36114	0.00672	0.04988	0.00070	0.8	0.01536	0.00027	309	5	313	6	344	4	308	5	-0.2	1.8	314	9	
	ARG27	Ju08b006	Mnz56	Core	High-Y	0.05027	0.00124	0.36285	0.00912	0.05020	0.00093	0.7	0.01609	0.00028	207	5	314	8	328	6	323	6	-4.4	1.6		
		Ju08b007	Mnz58	Core	Low-Y	0.05897	0.00139	0.42181	0.01010	0.05192	0.00090	0.7	0.01551	0.00026	566	13	357	9	326	6	311	5	8.7	4.7		
Ju08b0010		Mnz52	Rim-core	High-Y	0.05226	0.00123	0.37062	0.00886	0.05143	0.00089	0.7	0.01550	0.00026	297	7	320	8	323	6	311	5	-1.0	3.8	323	11	
Ju08b011		mnz52	Rim	Low-Y	0.08657	0.00204	0.62877	0.01503	0.05273	0.00092	0.7	0.01509	0.00025	1351	32	495	12	331	6	303	5	33.1	8.6			
3 Discordance calculated as (1-(206Pb/238U age/207Pb/235U age))*100																										
4 Discordance calculated as (1-(208Pb/232Th age/206Pb/238U age))*100																										